ChemComm

ROYAL SOCIETY OF CHEMISTRY

FEATURE ARTICLE

View Article Online
View Journal | View Issue

Cite this: *Chem. Commun.*, 2025, **61**, 6439

MXene-transition metal chalcogenide hybrid materials for supercapacitor applications

Gopinath Sahoo [a] and Chandra Sekhar Rout *[bc]

The rapid growth of technologies and miniaturization of electronic devices demand advanced the use of high-powered energy storage devices. The energy storage device are utilized in modern wearable electronics, stretchable screens, and electric vehicles. Due to their favorable electrochemical properties, nanomaterials have been used as electrodes for supercapacitors (SCs) with high power density, but they generally suffer from lower energy density than batteries. Compared to various nanomaterials, MXenes and transition metal chalcogenides (TMCs) have shown great potential for energy storage applications such as SCs. TMCs are gaining attention due to their stable electrochemical nature, adjustable surface activity, high electric conductivity, abundant chemically active sites, and stable cycling performance. However, the interlayer restacking and agglomeration of 2D materials limit their cycling performance. To overcome this, TMCs@MXene heterostructures have been developed, offering structurally stable electrodes with enhanced chemical active sites. In this review, we discuss recent advances in the development of different TMCs@MXene-based hybrids for the design of high performance SCs with improved specific capacitance, cycling life, energy density, and power density. The recent developments of this research field focusing on MXene-transition metal sulfides, MXene-transition metal selenides, and MXene-transition metal tellurides are elaborately discussed. Theoretical calculations carried out to understand the charge-storage mechanisms in these composites are reviewed. The importance of bimetallic TMCs and MXene heterostructure for enhanced energy storage is also highlighted.

Received 14th January 2025,
Accepted 24th March 2025

DOI: 10.1039/d5cc00223k

rsc.li/chemcomm

[a] *School of Basic Sciences, Indian Institute of Technology Bhubaneswar, Argul, Khordha 752050, India*
[b] *Centre for Nano and Material Sciences, Jain (Deemed-to-be University), Jain Global Campus, Kanakapura Road, Bangalore – 562112, Karnataka, India. E-mail: r.chandrasekhar@jainuniversity.ac.in, csrout@gmail.com*
[c] *Department of Chemical Engineering, Chungbuk National University, Cheongju, Chungbuk 28644, Republic of Korea*

Gopinath Sahoo

Gopinath Sahoo is a Postdoctoral researcher at the Indian Institute of Technology, Bhubaneswar, India, funded by NPDF, SERB, DST and working with Prof. Saroj Kumar Nayak. Prior to his current position, Dr Sahoo was a Brain-pool Postdoctoral Fellow (2021–2023) at Chungbuk National University, Chungbuk, South Korea, and worked with Prof. Sang Mun Jeong. He received his PhD degree in 2021 under the supervision of Prof. M. Kamruddin, from Indira Gandhi Centre for Atomic Research, Kalpakkam, a constituent institution under HBNI, affiliated to DAE, India. His current research work focuses on the development of electrode materials for energy-storage applications.

Chandra Sekhar Rout

Chandra Sekhar Rout is a full Professor at the Centre for Nano & Material Sciences (CNMS), Jain University. Before joining CNMS, He was a DST–Ramanujan Fellow at IIT Bhubaneswar, India (2013–2017). He obtained his PhD from JNCASR, Bangalore (2008) under the supervision of Prof. C.N.R. Rao, followed by postdoctoral research at NUS, Purdue University, and UNIST. His research is focused on applications of 2D layered materials for different devices. He has authored more than 200 research papers and 06 books. His h-index is 64 with total citations >16 000. He was ranked among the top 2% of scientists by the Stanford study in 2020–2024.

1. Introduction

The development of novel and high-performance electrode materials for electrochemical energy storage applications has received huge attention in recent years owing to the increasing need for renewable energy.[1–4] Due to their unique physical and chemical properties, including large surface area, structural and phase tunability, pore size distribution, and availability of abundant binding sites, 2D materials are gaining attention for energy applications.[5–10] Furthermore, their remarkable flexibility and good mechanical properties owing to their atomic structural arrangements make them suitable candidates for flexible energy storage devices and wearable electronics.[11–13] However, to date, no 2D material has demonstrated all the necessary properties to achieve high energy storage performance in terms of maximum energy/power density and cycle life. For example, in the case of graphene-based supercapacitors (SCs), the state-of-the-art capacity in non-aqueous electrolytes is reported to be less than 250 F g^{-1}, while the theoretical gravimetric capacitance is predicted to be over 550 F g^{-1}.[14,15] Having discovered in 2011, 2D MXenes have shown great promise for energy storage and SC applications due to their high electrical conductivity and excellent mechanical properties.[16] MXenes are generally represented by the chemical formula, $M_{n+1}X_xT_x$ (n = 1–4), where M represents the transition metal (Ti, Nb, V, and Mo), X denotes C/N/C_xN_y, and T_x represents the surface terminations (-OH, = O, and –F). Most of these MXenes are derived from their respective parent MAX phases by selective etching of the ''A'' layer, which usually consists of elements from groups 13–16 (Al and Si). Recently, MXenes have been vastly used in SC applications owing to their intrinsic high conductivity, hydrophilic surface, large surface area, variable oxidation states (because of the presence of transition metals in it) and pseudo-capacitive mechanism.[7,8,17–19] However, the layered structure of MXenes, formed *via* van der Waals interactions, undergoes inherent layer restacking into a dense structure during prolonged operation. Hence, this restacking tendency and aggregation limit their advantages for charge storage, hinder electrolyte ion movement and reduce the accessible surface area for electrochemical reactions. On the other hand, transition metal chalcogenides (TMCs) such as SnS, SnS_2, MoS_2, $MoSe_2$, WS_2, VS_2, VSe_2, VTe_2, $NiCo_2S_4$, $MnCo_2S_4$ and $NiMoS_4$ have emerged as promising electrode materials for SC applications. Their appeal lies in their earth abundance, low cost, tunable physicochemical properties, and variable oxidation state due to the presence of transition metals.[9,18,20–24] Hence, to tackle the restacking issues, the incorporation of TMCs with MXenes has gained significant attention in recent years.[18,25–28] The integration of TMCs with MXenes enhances the electrochemical activity and maintains a larger number of interlayer voids, facilitating ion movement through dual synergistic effects and resulting in overall improved structural integrity and electrochemical stability. Furthermore, fine-tuning and engineering the interlayer spacing in MXenes, along with optimizing the porosity of their hybrids, are necessary to promote charge transport capability, enhance electrolyte-accessible surface area, and achieve the predicted full charge storage performance.

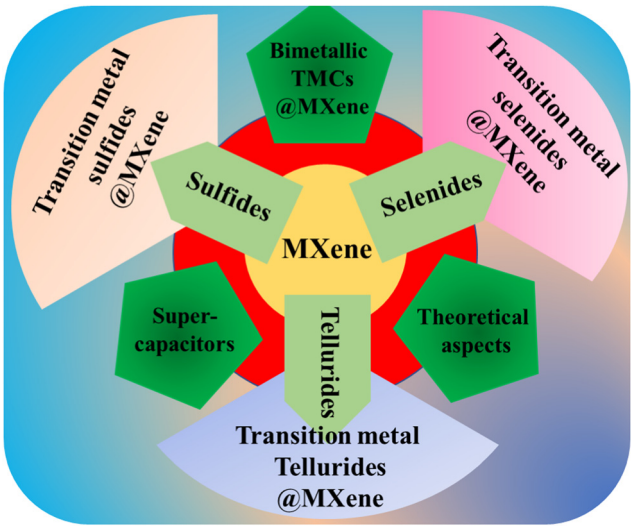

Fig. 1 Schematic showing the materials (TMCs@MXene) and key topics discussed in this review.

In this feature article, we discuss recent advances in TMCs@MXene-based materials for SC applications (Fig. 1), highlighting their improved energy storage performance in terms of capacitance, cycling life, energy density, and power density. We present recent developments in this research field carried out by our research group, with the sub-sections focusing on MXene-transition metal sulfides, MXene-transition metal selenides, and MXene-transition metal tellurides. Furthermore, the future perspectives and challenges of this emerging research field are discussed. The importance of bimetallic TMCs and MXene heterostructure for enhanced energy storage is noted. The theoretical calculations carried out to understand the charge-storage mechanisms in these composites are also discussed.

2. Design of MXene-based heterostructure for supercapacitors

Since MXenes are usually 2D layered materials, they act as ideal substrates, templates, or scaffolds for the growth of other nanomaterials (0D, 1D, and 2D) on their surface (Fig. 2). For example, a 0D MoS_2–Ti_3C_2 composite, prepared *via* electrostatic adsorption followed by its controlled growth using CTAB as the capping agent, effectively enhances electronic conductivity, facilitates Li^+ transport kinetics, and minimizes volume expansion.[29] Furthermore, 2D–2D heterostructures of WS_2-MXene, fabricated *via* a sonication-assisted procedure, prevent aggregation, while the WS_2 nano-spacers help to avoid the restacking of MXene sheets and increase the number of chemically active sites, leading to boosted energy storage performance.[30] Notably, 1D nanobeads of $NiCo_2S_4$ anchored on 2D MXenes prevent restacking through the confinement effect and the backing of electrostatic attraction between the materials.[31] The spinel $NiCo_2S_4$ grown on Ti_3C_2

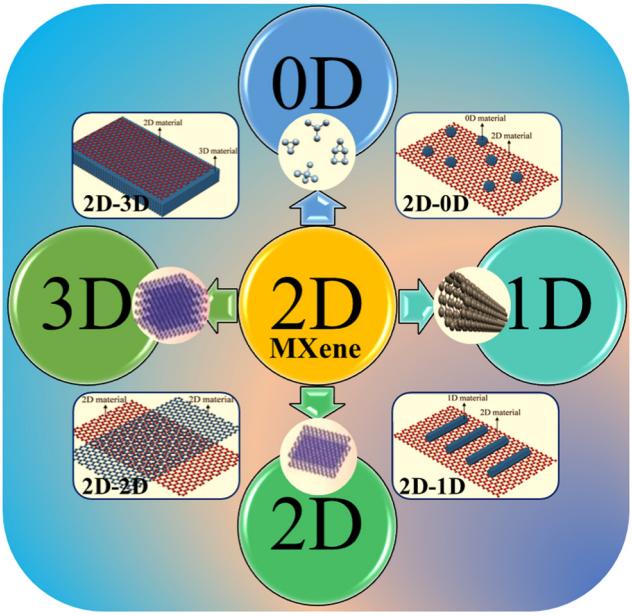

Fig. 2 Schematic of the classification of 2D MXene-based hybrids with nanomaterials of different dimensions (0D, 1D, 2D, and 3D) utilized for SC applications.

MXene sheets offers enhanced structural robustness and high mechanical strength, making it suitable for the fabrication of flexible SCs with high performance. Furthermore, precisely controlled and engineered morphologies, composition, interface structures, and interlayer spacing in 2D MXenes have been reported to effectively prevent restacking.[32,33] Radhakrishnan *et al.* demonstrated that ternary hybrids based on MXene-VTe_2-CNTs are viable electrode materials for flexible micro-supercapacitors, offering high capacity, outstanding rate capability, and long-term cycling stability.[32] The formation of MXene-based hybrids/heterostructures involves different mechanisms, including electrostatic interactions, hydrogen bonding, surface charges, covalent bonding, and combined hybrid forces.[25,34] Precise control over bonding, the selection of appropriate secondary material, experimental condition, and other assembly factors play crucial roles in fabricating MXene-based hybrid materials with exceptional properties suitable for SC applications.

The different heterostructures with MXene are discussed here, highlighting variations in their structures, interfaces, and interactions. For example, 0D nanomaterials such as nanoclusters and quantum dots of TMCs exhibit quantum confinement effects, which lead to excellent optical and electronic properties in 2D–0D MXene@TMC heterostructures. Furthermore, 1D nanomaterials such as nanorods, nanowires, and nanotubes of TMCs enable efficient electron transport in 2D–1D MXene@TMC heterostructures. Notably, 2D nanomaterials such as TMC nanosheets provide a high surface area, flexibility, and tunable electronic properties in 2D–2D MXene@TMC heterostructures. Additionally, 3D nanomaterials such as TMC nanoflowers provide a large surface area and enhanced mechanical strength in 2D–3D MXene@TMC heterostructures. Furthermore, the impact of interface interactions in different heterostructures is necessary for achieving excellent synergistic effects and enhancing material properties. The different heterostructures of MXene@TMC lead to enhanced performance, improved stability, increased conductivity, and tunable properties for energy storage applications. For instance, Chen *et al.* addressed the poor cycle stability and rate capability of pure MoS_2 electrodes by preparing MoS_2 on MXene heterostructures, which exhibited exceptional metallic properties.[35] In another example, Wang *et al.* resolved severe restacking, weak chemical immobilization ability, and poor catalytic effects of pure MXene by utilizing heterostructures based on $Ti_3C_2T_x$-TiN.[36] Hence, incorporating nanomaterials of different dimensions open up unique properties tailored for required applications. The transition metals used in the nanomaterials also have equal importance for property enhancement in the heterostructure.

3. Theoretical aspects of MXene-based supercapacitors

Theoretical simulation studies have predicted that MXenes have unique electrical and thermal conductivity, tunable electronic band gap, various magnetic ordering, low diffusion barriers, and high Young's modulus, which make them excellent candidates for high-performance energy storage device applications.[37–40] MXenes show promising energy storage performance in aqueous supercapacitors due to their metallic conductivity, which results from a high density of states at the Fermi level.[41] The layered structures of 2D MXenes allow rapid ion transport and provide more redox-active sites, making them ideal candidates for achieving high rates and long cycle life in SCs. Furthermore, the tunable properties due to the transition metal sites and surface functional groups favor both double-layer type capacitance and rapidly reversible redox reactions near or at the surface, leading to pseudo-type capacitance.[42] Pristine MXenes are predicted to show metallic conductivity due to the higher density of states (DOS) corresponding to M-d states near the Fermi level.[43] However, functionalization changes the electronic properties of MXenes, causing them to show characteristics ranging from metallic to semiconducting, depending on several factors, including the nature of the M, X, and T groups. Some MXenes, such as $(M'_{2/3}M''_{1/3})_2CO_2$ (M′ = Mo and W; M″ = Sc and Y), are predicted to become semiconductors after functionalization due to a shift in Fermi level, whereas most other MXenes retain their metallicity.[40] Theoretical calculations of the electronic band structure, band dispersion, and Fermi surfaces of OH-terminated MXenes show that the presence of nearly free electron (NFE) states near Fermi level, and their partial occupation contributes to higher electron conductivity by minimizing atomic scattering with surface vibrations.[44,45]

Theoretical calculations on MXenes towards charge storage mechanisms in different aqueous electrolytes provide important information for designing and optimizing the performance of the SC electrodes.[46,47] The dielectric constant of the electrolyte solvent, such as water molecules embedded between the

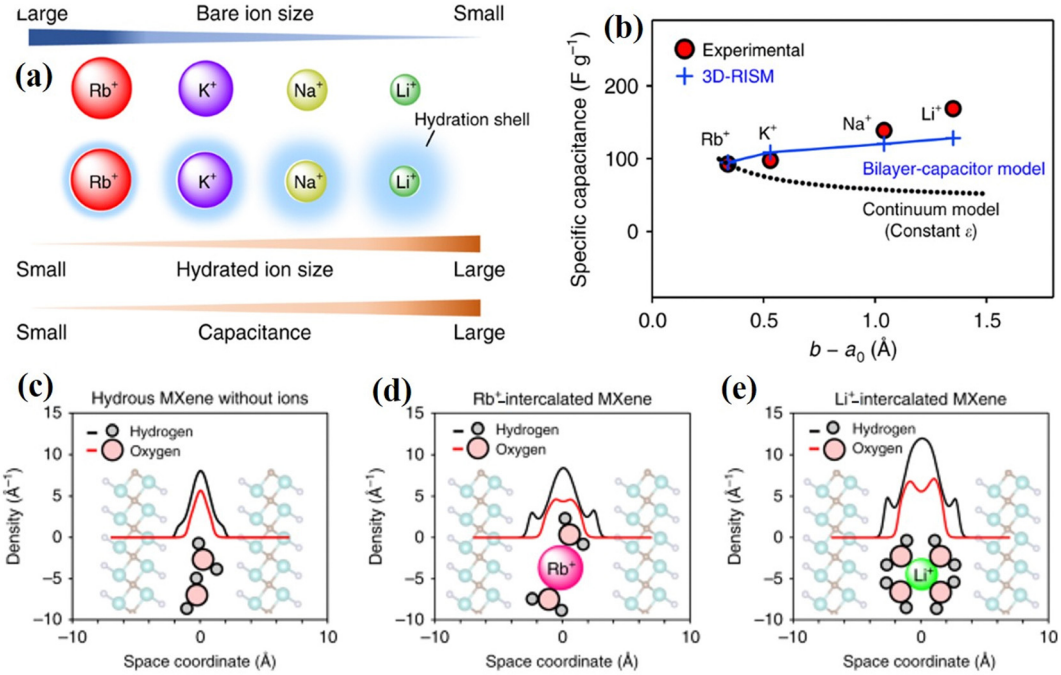

Fig. 3 (a) Orders of bare-ion size, hydrated-ion size, and observed capacitance, (b) dependence of ion-MXene distance ($b-a_0$) on the experimental specific capacitance, and (c)–(e) hydrogen and oxygen atomic density profiles along the c-axis (perpendicular to the MXene layers) in hydrous, Rb^+-intercalated, and Li^+-intercalated $Ti_2CT_x{\cdot}nH_2O$.[48]

MXene electrode and adsorbed ions, plays an important role in the performance of the devices due to the formation of the EDLC.[48] From a detailed comparative study, Sugahara *et al.* found that the capacity to accommodate larger amounts of water in MXene followed the order of $Li^+ > Na^+ > K^+ > Rb^+$, with the best energy storage performance observed in the case of Li^+ (Fig. 3a and b).[48] This trend, predicted *via* theoretical calculations for different ions, is attributed to the increasing hydration energy of cations ($Li^+ > Na^+ > K^+ > Rb^+$) as their bare ionic radii decrease (Fig. 3c–e).

Similarly, using DFT calculations, Ando *et al.* revealed that fully hydrated metal cation intercalation leads to the EDLC behavior of MXenes, with the hydrated shell shielding the orbital coupling between cation and MXene.[46] Furthermore, it has been reported that partially or completely de-solvated cations couple with the MXene electronic orbitals, leading to pseudo-capacitance. MXene-based electrodes are reported to exhibit higher capacitance in acidic electrolytes than alkaline (or neutral) electrolytes since protons undergo rapid redox reactions with the MXene surface. DFT calculations and the implicit solvation model for the surface of $Ti_3C_2T_x$ (T = O and OH) MXene in the H_2SO_4 electrolyte revealed the dominance of redox reactions over capacitance.[47] Furthermore, it was found that the proton redox process takes place between the −O site surface and interface water molecules, with the reaction rate being related to the number of intercalated water layers, and single-layer water exhibits the highest redox rate.

Different models are employed to estimate the theoretical capacitance values of MXene-based SCs, which helps in the design and optimization of newly emerging materials.[49–53] Ji *et al.* predicted that O-functionalized MXene in a neutral solution yields a capacitance of 56.6 F g^{-1}, and the integrated capacitance values of Ti_2CF_2 and Ti_2CO_2 in Na-ion capacitor are 291 F g^{-1} and 252 F g^{-1}, respectively (Fig. 4a and b).[49] As shown in Fig. 4c, the DOS and integral DOS aligned with the SHE are calculated to reflect the effect of terminations on the charge-storage ability of the Ti_3CNT_2 (T = F, O, or OH) monolayer. In the Ti_3CNO_2 monolayer, a large number of unoccupied partial density of states (PDOS) of Ti atoms above the Fermi level, in the range of an electrolyte window, indicates the enormous electronic capability of Ti atoms.[50] DFT combined with effective screening medium and reference interaction site model calculations revealed that depending on the halogen termination elements present in Ti_3C_2 MXene (with an order of I > Br > Cl > F), the EDLC values increased.[51] Smaller valence electron numbers of the terminating atoms with lower electronegativity facilitated the accumulation of electrons at the electrode surface (Fig. 4d). Molecular dynamics-based theoretical studies are employed to understand the transport processes of charge carriers in aqueous SCs to gain insights into the charge storage mechanisms of MXene-based electrodes.[54–56] These studies provide important information on the diffusion mechanisms of hydrated protons and electrolyte ions, migration energy barriers, and the effects of water molecules, with highly accurate insights into the molecular systems.

DFT calculations of TMCs/MXene-based SC electrodes provide insights into their electronic structure, orbital contribution, quantum capacitance, diffusion energy barrier, and induced voltage.[57–64] In the case of 1T VS_2@MXene hybrids, a lower diffusion energy barrier is observed compared to the pristine

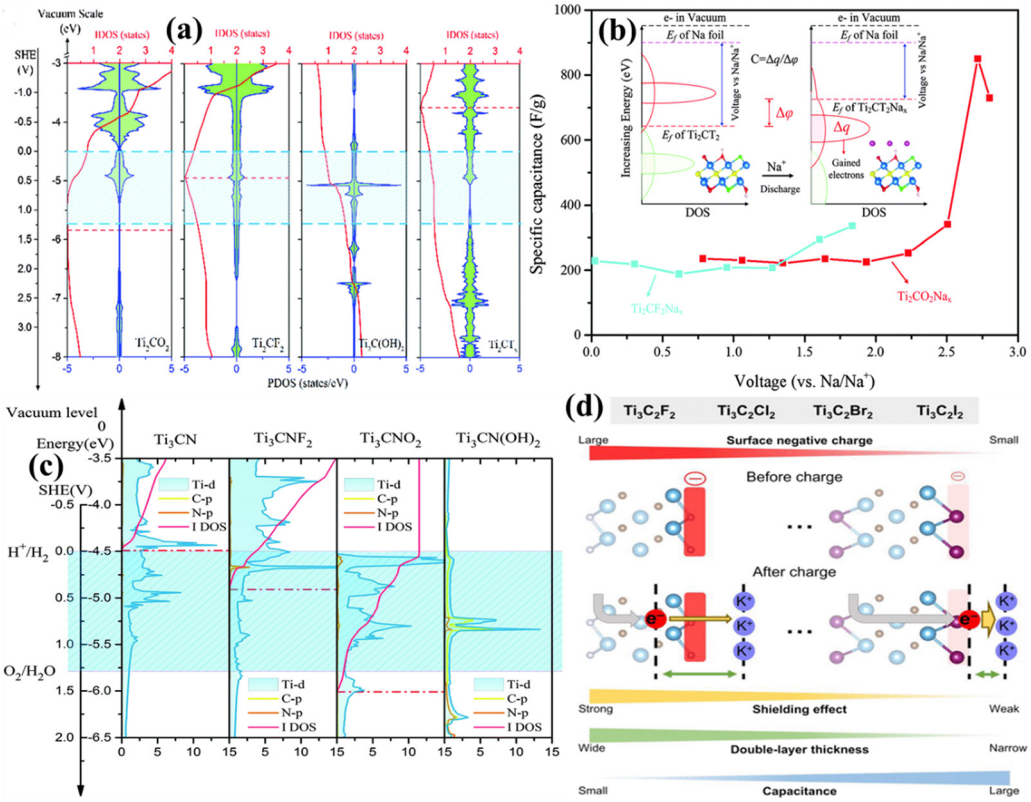

Fig. 4 (a) Relative dispositions of PDOS and integral DOS of the d-orbitals of Ti atoms in Ti_2CT_2 (T = O, F, and OH) and Ti_2CT_x nanosheets, (b) specific capacitance of Ti_2CO_2 and Ti_2CF_2 nanosheets,[49] (c) relative PDOS and integral DOS of the d-orbitals of Ti atoms referenced to the standard hydrogen electrode (SHE),[50] and (d) schematic showing the electronic impact of the MXene electrode surface on EDL capacitances depending on the surface functional groups.[51]

VS_2 and MXene.[58] Furthermore, the lower induced voltage at different concentrations of K^+ and the synergistic effect between the two materials mediated by the charge carriers from the Ti 3d orbitals of MXene to the 3p orbital of S in VS_2, contributes to achieving higher capacitance for the hybrid structure of VS_2@MXene. Similarly, in the case of β-SnS@MXene hybrids, charge transfer from the Ti 3d orbitals of MXene to the Sn 5p orbitals of the β-SnS surface contributes to the enhanced energy storage performance of the composite (Fig. 5).[57] The discrepancy in the work function between β-SnS (5.37 eV) and MXene (3.90 eV) creates an inherent electric field facilitating electron transfer from MXene to β-SnS (111) surface, which is found to be the cause for the growth, stability, and enhanced performance of the material. The large surface area of β-SnS (111)@MXene nanocomposites and the charge transfer processes produce additional states in the density of states near the Fermi level, significantly contributing to the better charge storage performance of the SCs. In the case of MXene-TMC-based ternary hybrids, such as $MoWS_2$@BCN@$Ti_3C_2T_x$, theoretical calculations suggested the interlayer interactions and charge transfer from the Mo 4d orbitals of $MoWS_2$ and the C 2p orbitals of BCN to the C 2p orbitals of MXene are the primary driving forces behind the enhanced energy storage performance.[59] DFT calculations provided important information on the quantum capacitance calculations of B-doped 1T-MoS_2 hybridized with $Ti_3C_2T_x$ and validated the experimental observations of its charge storage performance.[60] Similarly, it is predicted that metal selenides such as $NiCoSe_2$, $CrSe_2$, and VSe_2 hybridized with MXene show higher quantum capacitance values than their pristine counterparts, supporting the experimental findings.[61–63] In the case of $CrSe_2$@MXene, the calculated work function is found to be reduced to 4.49 eV compared to the pristine $CrSe_2$ (5.66 eV) due to the creation of defects (Fig. 6).[62] Further calculations and Bader charge analysis show that quantum capacitance values are higher for the hybrids due to contributions from the created defects and an enhanced density of states near the Fermi level. For VTe_2@$Ti_3C_2T_x$ MXene, DFT calculations predicted an enhancement of electronic Te 5p states near the Fermi level because MXene led to boosted performance.[64]

4. MXene and transition metal chalcogenide hybrids for supercapacitor applications

MXenes and TMCs have wide applications such as energy storage, energy conversion, sensors, and catalysts. Although the individual materials show a lack of potential in terms of electrical conductivity, surface area, cycle stability, and rate

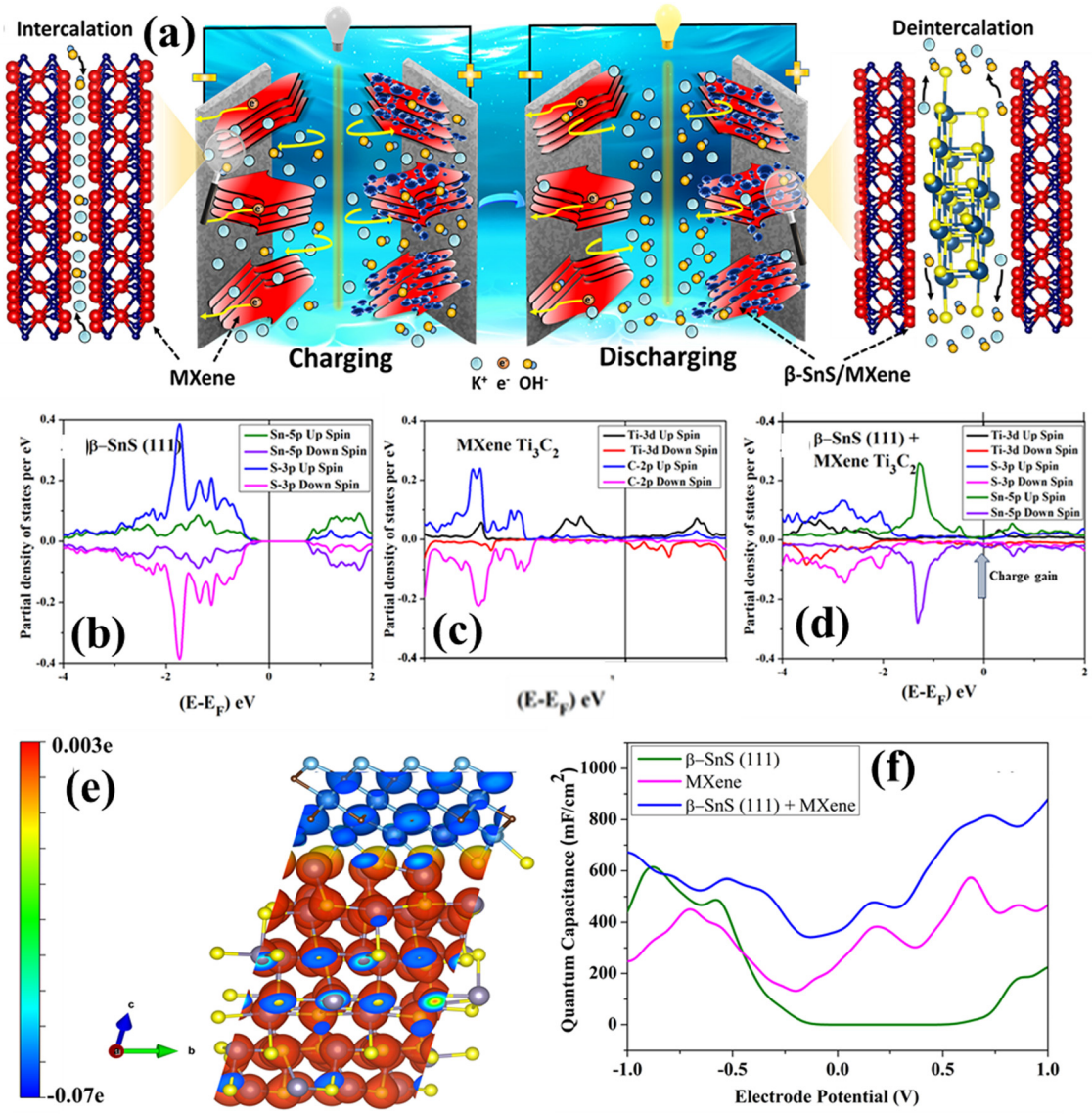

Fig. 5 (a) Schematic of the charge storage mechanism in the device. (b) Sn-5p and S-3p orbitals of the β-SnS (111) surface, (c) Ti-3d and C-2p orbitals of MXene, and (d) Ti-3d, Sn-5p, and S-3p orbitals of the β-SnS@MXene (111) heterostructure. Yellow, purple, sky blue, and brown spheres represent S, Sn, Ti, and C atoms, respectively. (e) Surface charge density difference plot for the β-SnS@MXene (111) heterostructure and MXene for an isosurface value of 0.063e. (f) Comparison of the differential quantum capacitance of β-SnS (111), MXene, and β-SnS (111)@MXene heterostructure for the local electrode potential.[57]

capacitance, their uniformly stacked layers help them achieve high energy-density SCs. Generally, the goal is to enhance the electrical conductivity of TMCs and prevent the restacking of MXene by preparing TMCs@MXene composites. A single material exhibiting the required properties for an application is quite impossible, hence developing composite materials with suitable and tuned properties to complement their quality and enhance overall performance is preferred. The advantage of these composites include enhanced electrochemical activity, large interlayer voids for ion movement, and synergistic effects that improve structural and electrochemical stability. However, there are some drawbacks: (i) MXenes and TMC are not thermally stable, (ii) agglomeration of TMC particles can lead to bulk structures that reduce their active surface area and ion diffusion pathways, and (iii) some materials in the composites may be weakly bonded during synthesis, leading to material instability during electrochemical cycling. Additionally, there are challenges with TMCs@MXene composites, including synergistic interactions, compatibility, stability, scalability, and interfacial bonding. Effective synergistic interactions between MXenes and TMCs in hybrid systems can be complex and require careful design. The compatibility and stability of the materials are crucial for long-term performance within a hybrid structure. The synthesis procedures currently produce a less amount of active materials, so further optimizations are required to scale up the production of TMCs@MXene hybrid materials while maintaining their properties and performance. Poor interfacial interactions between MXenes and TMCs in the

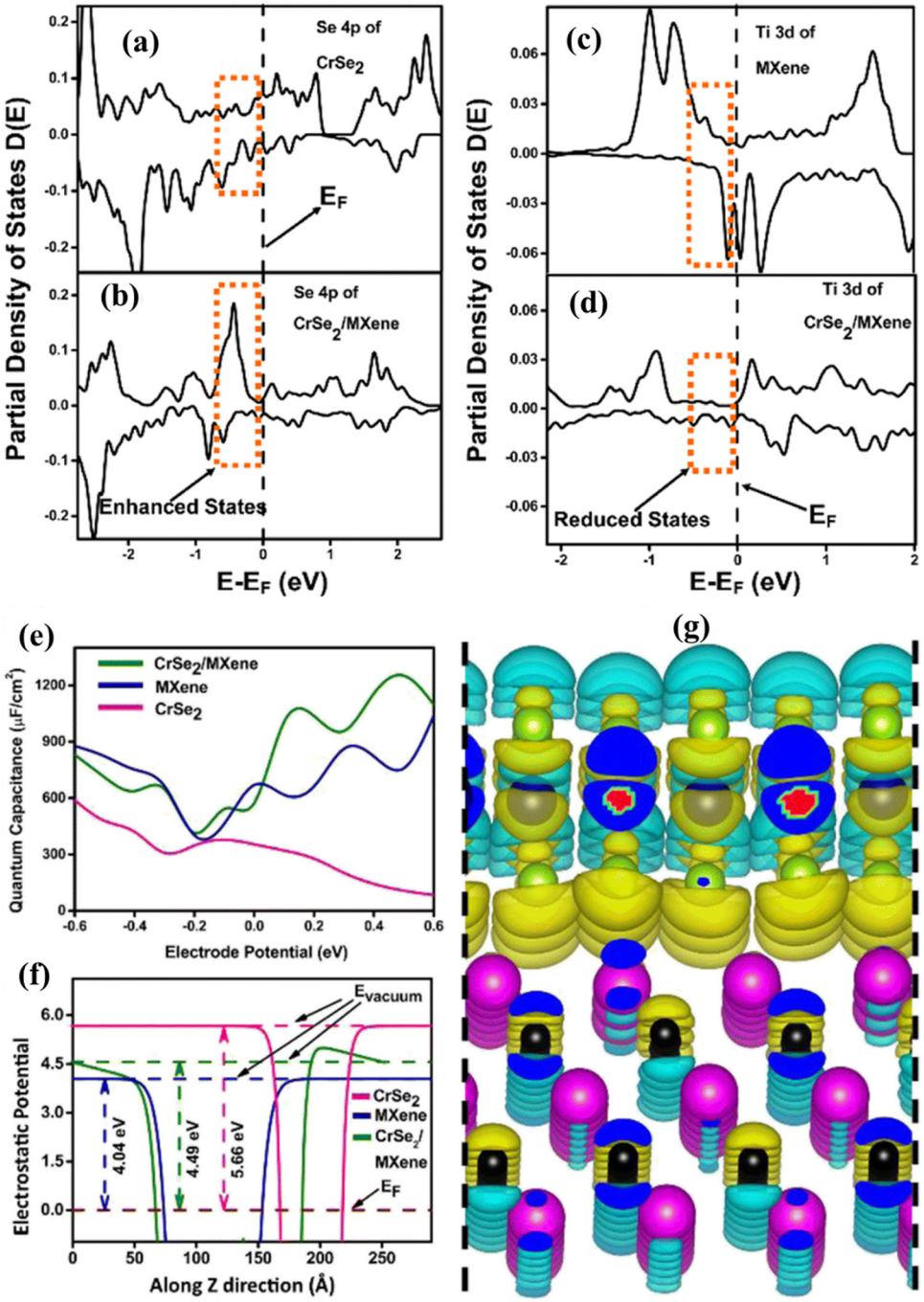

Fig. 6 Partial density of states: (a) and (b) partial density of states of the Se 4p orbital of $CrSe_2$ and the Se 4p orbital of $CrSe_2$@MXene and (c) and (d) plots of the Ti 3d orbital of MXene and Ti 3d orbital of $CrSe_2$@MXene. Quantum capacitance and work function: (e) quantum capacitance *versus* applied voltage for $CrSe_2$, MXene, and $CrSe_2$@MXene, (f) plot of the work function of $CrSe_2$, MXene, and $CrSe_2$@MXene, and (g) visualization of the charge density difference between MXene and $CrSe_2$.[62]

hybrid material can lead to reduced performance. Some of the problems and difficulties associated with TMCs@MXene hybrids have been addressed recently by various research groups, which are discussed here. TMCs based on sulfides, selenides, and tellurides, when combined with MXenes, are being studied for energy storage applications. TMCs consist of a metallic component (transition metals) and chalcogens (S, Se, or Te) to form compounds with a wide range of properties, including semiconducting, metallic, and even superconducting characteristics. There are different possible chemical compositions according to the metallic composition, which forms monometallic TMCs (MX, where M is a transition metal and X is chalcogens) and bimetallic TMCs (M_1M_2X, where M_1 and M_2 are transition metals and X is chalcogens). Monometallic

TMCs (MTMCs) are stable but depend on the specific transition metals, whereas bimetallic TMCs (BTMCs) exhibit higher stability due to the presence of two metals. MTMCs exist in the MX or MX_2 form. Zinc sulfide, for example, is one of the MTMCs in the MX form, where the sulfide atoms pack in cubic symmetry, and Zn^{2+} occupy half of the tetrahedral holes. MTMCs with the MX_2 structure are covalently bonded, where a single metal atom layer sandwiched between two chalcogens atom layers. MoS_2, WS_2, $MoSe_2$, WSe_2, and $MoTe_2$ exhibit a direct band gap and can be used in electronic applications. The strong spin–orbit coupling in MX_2 type MTMCs leads to a spin–orbit splitting of several hundred meV in the valence band and a few meV in the conduction band, which allows for the control of the electron spin by tuning the excitation laser photon energy. BTMCs ($M_1M_2X_4$ or $M_1(M_2)_2X_4$) exhibit diverse bonding types, including ionic, covalent, or metallic due to the presence of two metals. Their various oxidation states, improved electrochemical activity, increased electronic conductivity due to a reduced band gap, and higher structural stability are the reasons for their application in energy storage. Furthermore, the metals play a crucial role in the properties of the TMCs. For example, the ternary $NiCo_2S_4$ outperforms $NiCo_2O_4$, as well as single-component Ni and Co oxides and sulfides, with its higher conductivity and more complex redox chemistry, making it highly valuable for applications.[65] For future directions, heterostructure composites of MTMCs and BTMCs ($NiCo_2S_4/MoS_2$, $CuCoS_4/WS_2$, and $CoNi_2Se_4/SnS_2$) can be explored. In this section, a detailed discussion of different TMCs and MXene composite materials for SC application are discussed.

4.1. MXene and transition-metal sulfides

Transition metal sulfides are generally layered metal sulfides, where one metal layer is present between the two sulfur layers. These layers are bonded *via* weak van der Waals force.[66] MoS_2, SnS_2, WS_2, *etc.* are examples of metal sulfides with layered structures. Furthermore, the layered metal sulfides are represented by *n*X, where *n* is the number of layers, and X is the structural phase of the material. Examples of these phases include IT, 2H, and 3R, which represent single-, bi-, and trilayered tetragonal, hexagonal, and rhombohedral structures, respectively.[67] Non-layered metal sulfides also exist, where the chemical bonding between the metals and sulfur atoms occurs in an octahedral arrangement. Due to their high theoretical capacitance, variable oxidation states, low cost, superior redox reversibility, and ease of synthesis, transition metal sulfides are potential candidates for SC applications.[68,69] Transition metal sulfides such as VS_2, CoS, CoS_2, Co_3S_4, NiS, Ni_3S_4, CuS, MoS_2, SnS, SnS_2, and WS_2, are vastly use for SC applications.[58] However, the self-restacking and aggregation of layered metal sulfides have prompted efforts to enhance the electrochemical performance by forming hybrids structures with MXene. In MXene-transition metal sulfide composites, the engineered layered structure depicts excellent properties, including improved conductivity, large specific surface area, and numerous ion-accessible active chemical sites.[21,69] Furthermore, binary transition metal sulfides such as $MoWS_2$, NiCoS, $NiCo_2S_4$, Co_2CuS_4, ZnCoS, and MnCoS combined with MXenes are extensively used in SCs, where the synergistic effect of bimetals enhances the charge-storage performance.[70–74]

The unique 2D structure of vanadium sulfides provides better charge-transfer kinetics and ion mobility. 1T-VS_2@MXene hybrid electrode materials, such as 2D–2D type heterostructure material, were synthesized by Sharma *et al.*[58] by optimizing with different concentrations of MXene. The VS_2-MX-50, where 5 mg mL^{-1} of MXene was added to form the optimized composite, showed the highest specific capacitance of 106.38 F g^{-1} at 0.2 A g^{-1}. The mass loading of the active material was maintained at 2 mg in the electrode. The comparative CV and CD profiles of different 1T-VS_2@MXene are shown in Fig. 7a and b. To understanding the charge storage nature, the hybrid structure and its total density states (TDOS) are plotted in Fig. 7c and d, respectively. Due to the addition of MXene, an enhancement of electronic states near the Fermi level is observed. The hybrid 1T-VS_2@MXene shows a lower diffusion energy barrier for electrolytic ions, which supports the increase in charge storage. Both effects—the enhanced density of states and lower diffusion barrier—explain the better charge storage performance of the 1T-VS_2@MXene hybrid. Furthermore, the asymmetric supercapacitor VS_2@MXene// MXene was fabricated with an operating potential of 1.6 V. The highest energy density achieved was 41.13 W h kg^{-1} at a maximum power density of 793.50 W kg^{-1}. Similarly, Chen *et al.*[75] reported a VS_2@MXene composite prepared *via* a hydrothermal process, forming a 2D–2D-type heterostructure, which showed a specific capacitance of 1791.4 F g^{-1} (895.7 C g^{-1}) at 1 A g^{-1}, with high rate capability (1175 F g^{-1}) at 20 A g^{-1} (Fig. 7f), where the mass loading of the active materials was approximately 5 mg cm^{-2}. The comparative CV of MXene, VS_2, and VS_2@MXene is given in Fig. 7e, which depicts a high area under the curve for the hybrid composite. Moreover, the solid-state asymmetric supercapacitor device VS_2@MXene//Fe_3O_4@rGO was fabricated, showing a specific energy of 73.9 W h kg^{-1} at a specific power of 728.2 W kg^{-1}, with 90.7% capacity retention after 10 000 cycles at 8 A g^{-1}. Furthermore, the discharge time of the device was found to be higher in the case of the parallel configuration confirmed by the respective CD profile (Fig. 7g) and validated by blue LED illumination (Fig. 7h). Wang *et al.* proposed a flower-like VS_2 decorated on Ti_3C_2 MXene, forming a 2D–3D-type heterostructure, which showed an increase in electrical conductivity, and a specific capacity of 191.3 mA h g^{-1} at 1 A g^{-1}, with 91.6% capacity retention over 5000 cycles at 2 A g^{-1}, and the mass loading on the electrode was 1–2 mg cm^{-2}.[76] Moreover, incorporating carbon materials into the TMC@MXene composites supports the structure, increasing electrochemical activity and durability. The optimized VS_2@MXene@CNT 2D–2D/1D-type heterostructure composite was prepared using the hydrothermal method with 50 mg of MXene.[77] The details of the synthesis method are depicted in Fig. 7i. The hybrid composite, with a mass loading of 2 mg on the electrode, achieved a specific capacitance of 505 F g^{-1} at 0.2 A g^{-1}, with excellent rate capability (Fig. 7j). Furthermore, the composite showed 89.2% capacitive contribution at 20 mV s^{-1}, calculated from the current–voltage

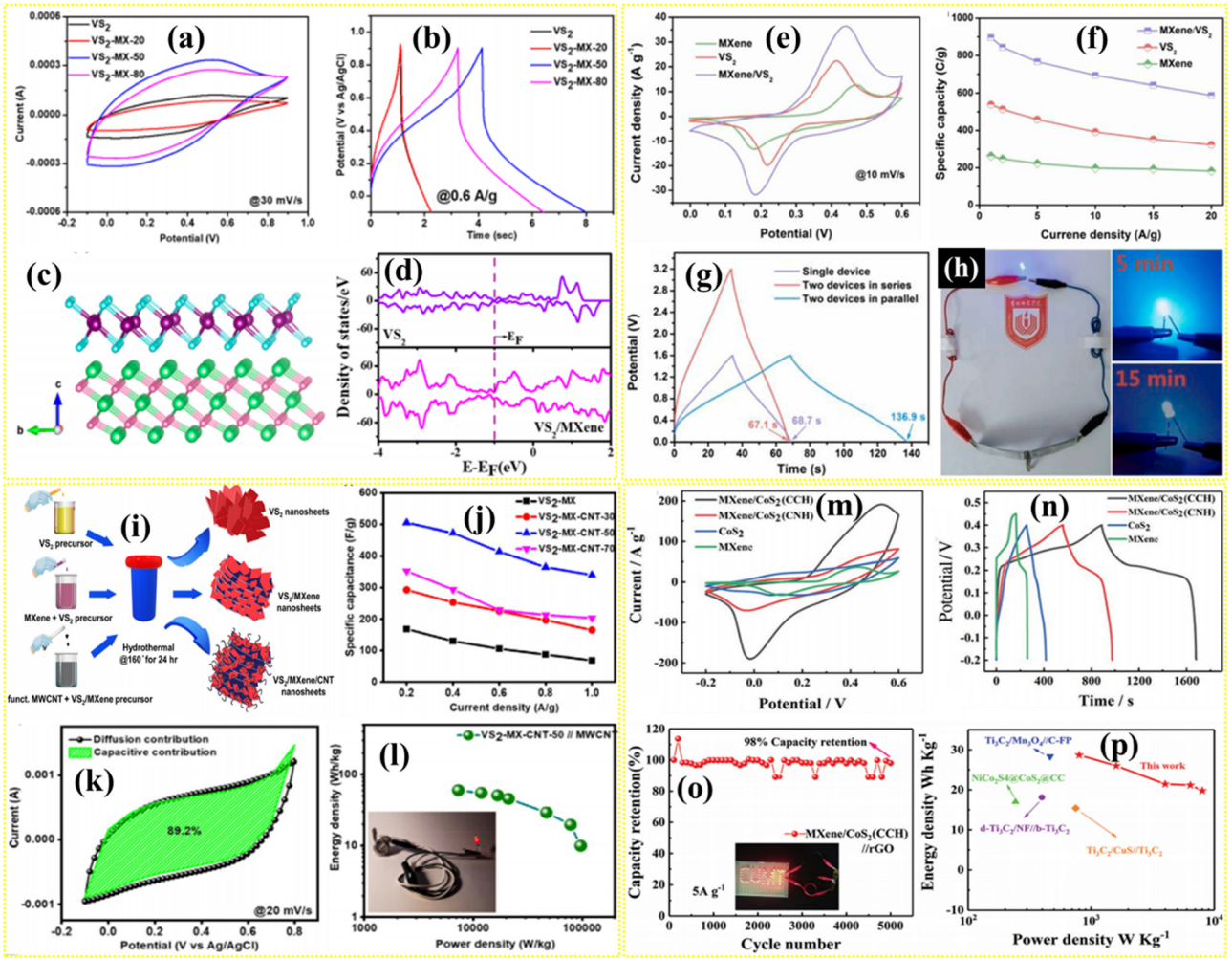

Fig. 7 (a) Comparative CV curves of VS_2 and different VS_2@MXene at a scan rate of 30 mV s^{-1}, (b) comparative CD curves of VS_2 and different VS_2@MXene at a current density of 0.6 A g^{-1}, (c) side view of VS_2@MXene with the (001) layer of 1T-VS_2 and the (002) layer of MXene; purple, cyan, pista green, and pink colors represent V, S, Ti, and C atoms, respectively, and (d) TDOS plot for 1T-VS_2 and VS_2@MXene.[58] Comparative (e) CV curves and (f) rate capability of VS_2, MXene, and VS_2@MXene. (g) CD profiles of two VS_2@MXene//Fe_3O_4@rGO devices connected in series and parallel configurations. (h) Photographs of blue LED illumination.[75] (i) Schematic of the synthesis procedure and (j) rate capability for VS_2, VS_2@MXene, and VS_2@MXene@CNT. (k) Capacitive- and diffusion-controlled charge-storage contributions for VS_2@MXene@CNT. (l) Ragone plot demonstrating the energy and power density of the device, with insets showing the LED illumination.[77] Comparative (m) CV and (n) CD profile of CoS_2@MXene with pristine samples. (o) Cycle stability, with inset showing LED test, and (p) Ragone plot of the device.[79]

equation (Fig. 7k). Hence, the incorporation of MXene and CNT increases the number of surface active sites, further enhancing surface activity and capacitive contributions due to their synergistic effect. The VS_2@MXene@CNT//CNT device was also designed to achieve an energy density of 59.85 W h kg^{-1} and a maximum power density of 7303.72 W kg^{-1}, with a wide 1.7 V potential window (Fig. 7l). The performance of an asymmetric SC device using VS_4 and MXene as electrodes was studied by Sharma *et al.* in a working potential of 1.3 V.[78] The device VS_4//MXene showed an areal capacitance of 70.9 mF cm^{-2} at 5 mV s^{-1}, with 75% cycle stability over 3000 cycles, which is 4.5 and 6 times higher than the VS_4 and MXene symmetric devices, respectively. VS_4 showed a lower diffusion barrier, leading to better charge kinetics, which improved the charge storage performance. Cobalt disulfide exhibits high specific capacity and contains active redox site, making it suitable for SC applications. However, the material undergoes volume expansion during charge storage, which can be avoided by forming a suitable composite with MXene. Liu *et al.*[79] synthesized CoS_2@MXene composites in a 2D–0D heterostructure separately using cobalt chloride hexahydrate (CCH) and cobalt nitrate hexahydrate. The CoS_2@MXene synthesized with CCH exhibited improved capacitance performance, achieving 1320 F g^{-1} at 1 A g^{-1}, as confirmed by the comparative CV and CD shown in Fig. 7m and n. The CoS_2 nanoparticles decorated on MXenes importantly increased the chemically active sites of metal ions during redox reactions. Moreover, the CoS_2@MXene//rGO asymmetric SC device, with a total mass loading of 5.8 mg of active materials, exhibited a high energy density of 28.8 W h kg^{-1} at a power density of 800 W kg^{-1}, along with 98% of specific capacitance retention

after 5000 cycles at 5 A g^{-1} (Fig. 7o and p). Pan *et al.*[80] reported the CoS_2@MXene//rGO device, which exhibited a higher energy density than the CuS@Ti_3C_2//Ti_3C_2 device (15.4 W h kg^{-1}).

The transition metal nickel sulfide has abundant availability as raw material, high theoretical specific capacity, and good conductivity, making it a promising material for energy storage applications. Furthermore, when combined with MXene, the composite shows better rate capability and cycle stability. Liu *et al.*[81] prepared a flower-like NiS on $Ti_3C_2T_x$, forming a 2D–3D-type heterostructure through a single-step hydrothermal process, as shown in the schematic of the synthesis procedure (Fig. 8a). The optimized NiS@MXene composite demonstrated a specific capacity of 554.1 mA h g^{-1} (857.8 F g^{-1}) at 1 A g^{-1}, which is four times higher than that of pristine MXene. The NiS nanoflakes formed voids in the layered structure of the MXene, facilitating better transfer of ions and charges. The comparative CV (−0.2 to 0.8) and CD profiles are depicted in Fig. 8b and c, respectively. The larger area under the CV curve and the longer discharge time in the CD profile imply the improved capacitance of the optimized composite. The specific capacities of other composites with varying Ni compositions were reported as 392.4 mA h g^{-1}, 471.7 mA h g^{-1}, and 130.3 mA h g^{-1}. The asymmetric device NiS@MXene//Graphene@AC exhibited 97.7% capacitance retention after 3000 cycles, with an energy density of 17.688 W h kg^{-1} at a power density of 750 W kg^{-1}. Similarly, the NiS@Ti_3C_2 composite, prepared in a 2D–0D-type heterostructure configuration, delivered a specific capacity of 840.4 C g^{-1} at 1 A g^{-1} with 64% retention in capacity. In this study, the mass loading of the active material was approximately 2.1 mg cm^{-2}.[82] The superior performance is attributed to the presence of electric channels in the MXene, which enhance electron transport at the interface of the composite, and the increased surface area, which boosts the number of redox-active sites at the composite. Another form of nickel sulfide, Ni_3S_2, is also notable due to its low cost, driven by the availability of natural minerals, and its high theoretical specific capacitance. Zhao *et al.*[83] synthesized a 2D–2D heterostructure of Ni_3S_2@Ti_3C_2, confirmed by TEM micrograph (Fig. 8d) and the (003) planes of Ti_3C_2 with a plane separation of 0.24 nm (Fig. 8e). The composite, with a mass loading of 1.5 mg, exhibited a specific capacitance of 2204 F g^{-1} at 1 A g^{-1} compared with pristine Ni_3S_2 and MXene. The rate capability plot provided in Fig. 8f depicts 60% capacity retention at 10 A g^{-1} for the composite. The hybrid Ni_3S_2@MXene//AC device exhibited an energy density of 23.6 W h kg^{-1} and a maximum power density of 4004.4 W kg^{-1}, with 76.7% capacity retention after 5000 cycles (Fig. 8g). Copper sulfide (CuS) is an attractive TMC for various energy storage applications due to its metal-like electronic conductivity and chemical stability. Furthermore, combining CuS with MXene enhances the properties and surface area of materials, leading to improved electrochemical

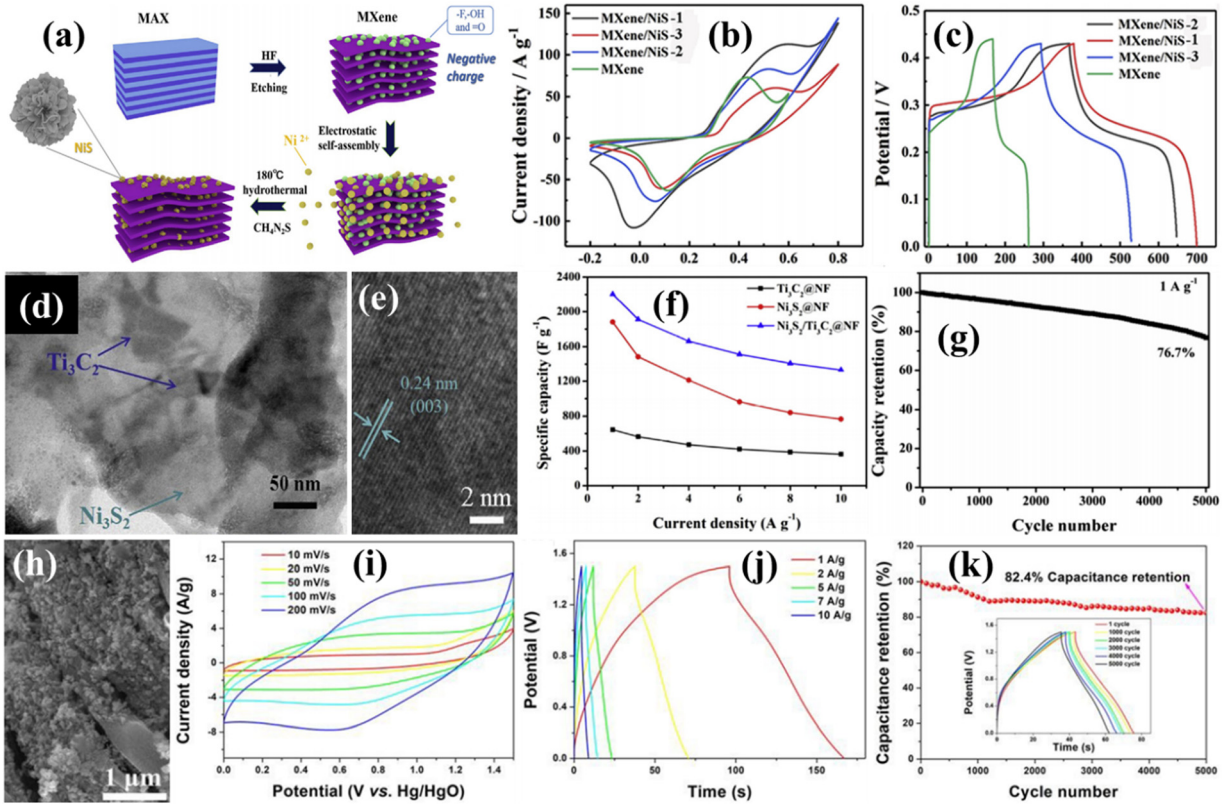

Fig. 8 (a) Schematic of the synthesis procedure for NiS@MXene. Comparative (b) CV and (c) CD profiles of the NiS@MXene composites.[81] (d) TEM and (e) HRTEM images of Ni_3S_2@MXene. (f) Rate capability curves (change in specific capacity with current density) comparison of Ni_3S_2@MXene with only MXene and Ni_3S_2, and (g) cycle stability of the hybrid Ni_3S_2@MXene//AC device.[83] (h) SEM image of CuS@MXene. (i) CV curves, (j) CD curves, and (k) capacitance retention of the CuS@MXene//MXene device, with inset comparing CD curves at 1st, 1000th, 2000th, 3000th, 4000th, and 5000th cycle.[80]

capacitance. 2D Ti_3C_2 decorated with a CuS nanoparticle in a 2D–0D type heterostructure was reported by Pan *et al.*,[80] in which the nanoparticles were uniformly distributed in the composite (Fig. 8h). The CuS@MXene composite, with a mass loading of 2.5 mg cm^{-2}, showed a specific capacity of 169.5 C g^{-1} at a current density of 1 A g^{-1}, approximately five times higher than that of Ti_3C_2. The boost in capacity is due to the synergistic effects of the excellent electronic conductivity of Ti_3C_2 and the better electrochemical activity of CuS. The CuS@MXene//MXene device showed favorable CV and CD characteristics at different scan rates and current densities, respectively (Fig. 8i and j). The device achieved a high energy density of 15.4 W h kg^{-1} at a power density of 750.2 W kg^{-1}, with 82.4% capacity retention maintained after 5000 cycles at 2 A g^{-1} (Fig. 8k).

Notably, 2D transition-metal dichalcogenides (TMDs) are TMCs that are characterized by variable oxidation states, unique sheet-like morphology, and large surface area with rich physio-chemical properties. MoS_2 is one such TMC, known for its layered structure, enhanced ionic conductivity, and large interlayer spacing. However, MoS_2 also has drawbacks such as low mass transport rate and poor electrical conductivity, which inhibit its electrochemical performance. Hence, forming a heterogeneous 2D layered hybrid structure of MoS_2 and MXene can enhance its properties, resulting in excellent supercapacitance performance. Several research groups have studied MoS_2@MXene composites and their modified structures for SC applications.[60,84–87] Kirubasankar *et al.*[84] reported MoS_2@MXene composites in a 2D–2D type heterostructure, achieving a specific capacitance of 583 F g^{-1} at 1 A g^{-1} with a rate capability of 82.5% compared to the pristine materials. The mass loading was maintained at 2.5 mg cm^{-2} in this work. The comparative CD profiles at 2 A g^{-1} are depicted in Fig. 9a. The reported hybrid device MoS_2@MXene//$Ni(OH)_2$ exhibited an active potential window of 1.6 V (Fig. 9b) and consistent CV curves across a scan rate range of 5 to 100 mV s^{-1} (Fig. 9c). Furthermore, the device showed an energy density of 54 W h kg^{-1} at a power density of 0.86 kW kg^{-1}. The MoS_2@MXene hybrid structure in a 2D–2D configuration, reported by Chandran *et al.*,[85] showed a specific capacitance of 342 F g^{-1} at a current density of 0.4 A g^{-1}, with a maintained mass loading of 1.5 mg cm^{-2}. A mixed-dimensional MoS_2@MXene in a 2D–2D/3D heterostructure, synthesized by Hou *et al.*,[86] showed accelerated electron transfer and reduced aggregation of MoS_2, resulting in improved electrochemical performance. The composite, with a mass loading of 5 mg cm^{-2}, achieved a specific capacitance of 303.8 F g^{-1} at a current density of 1 A g^{-1}, which was five times higher than that of MoS_2 and three times higher than MXene alone. The symmetric SC device exhibited a specific capacitance of 115.2 F g^{-1} at 0.5 A g^{-1}, with 72.3% capacitance retention after 10 000 cycles, and delivered a high energy density of 5.1 W h kg^{-1} at a power density of 298 W kg^{-1}. Furthermore, a porous MoS_2@MXene hybrid structure in a 2D–3D configuration was synthesized. The electrodes were tested with mass loading ranging from 0.25 to 0.75 mg cm^{-2}. The composite displayed a specific capacitance of 439 F g^{-1} at 5 mV s^{-1} and demonstrated long-term cycle stability. The symmetric device retained 91% of its capacitance after 10 000 cycles of repeated charge and discharge.[87]

Furthermore, incorporating heteroatoms into the material changes the structure and intrinsic properties of the composite. These property changes result from defects, lattice distortion, and bond modifications, which affect the electron properties of the material. Hence, extensive research has been carried out, where heteroatom is doped or incorporated into TMCs or MXenes to improve material properties and, hence, electrochemical performance. Boron-modified 1T-MoS_2@MXene in a 2D–2D heterostructure enhances the charge-storage performances of the composite because boron activates the basal planes in the structure.[60] Simulation studies also support these findings, indicating that hybridization with $Ti_3C_2T_x$ and B substitution enhances the conductivity of the 1T-MoS_2 system. The detailed micro-SC fabrication process is given in Fig. 9d. The composite electrode demonstrated a capacitance of approximately 420 F g^{-1} in a two-electrode system and an areal capacitance of 72.31 mF cm^{-2} in a symmetric micro-SC configuration. The charge storage process is primarily capacitive, and the detailed electrochemical reactions involved are given in Fig. 9e. Similarly, MXenes can also be modified for enhanced performance. Nitrogen-doped MXenes were used to synthesize MoS_2@N-MXene-carbon in a 2D–2D heterostructure, which exhibited a specific capacity of 189 mA h g^{-1} at 4 A g^{-1} when used as an anode material in Na-ion batteries. The mass loading was estimated to be 1–1.5 mg cm^{-2}.[89] Furthermore, tin sulfides (SnS), known for their high electron mobility and theoretical capacitance, are promising electrode materials. SnS exists in different crystal phases, especially α, β, and π phases. Patra *et al.*[57] studied the effect of different SnS phases in SnS@MXene composites (2D–0D type heterostructure) on their electrochemical performance. β-SnS@MXene showed a comparatively higher capacitance of 615 mF cm^{-2} at a flow rate of 4 mA cm^{-2} compared to α-SnS and π-SnS. The improved performance is due to charge transfer from the Ti 3d orbitals of MXene to the Sn 5p orbitals of the β-SnS surface, as confirmed by the partial density of states analysis. The CV profile of the optimized β-SnS@MXene is given in Fig. 9f. Furthermore, the hybrid SC β-SnS@MXene//MXene displayed a high areal capacitance of 109 mF cm^{-2}, along with an energy density of 34.06 μW h cm^{-2} at a power density of 6.28 mW cm^{-2} (Fig. 9g and h). WS_2 typically shows poor capacitance and weak electronic conductivity; however, its electrochemical performance can be substantially enhanced by forming a potential composite with MXene. The specific capacitance enhanced after inserting 1T-WS_2 nanospacers into the matrix of MXene, forming a 2D–1D heterostructure synthesized *via* a sonication-assisted method.[30] The WS_2@MXene composite, synthesized in a 2D–2D heterostructure *via* a hydrothermal method, exhibited a specific capacitance of 373 F g^{-1} at 0.4 A g^{-1}, which is substantially higher than WS_2 (47 F g^{-1} at 0.4 A g^{-1}) and MXene (71 F g^{-1} at 0.4 A g^{-1}).[90] The EIS results indicated a low charge transfer resistance of 2.29 Ω for the composite, which enhances charge kinetics and overall performance. Furthermore, incorporating carbon materials

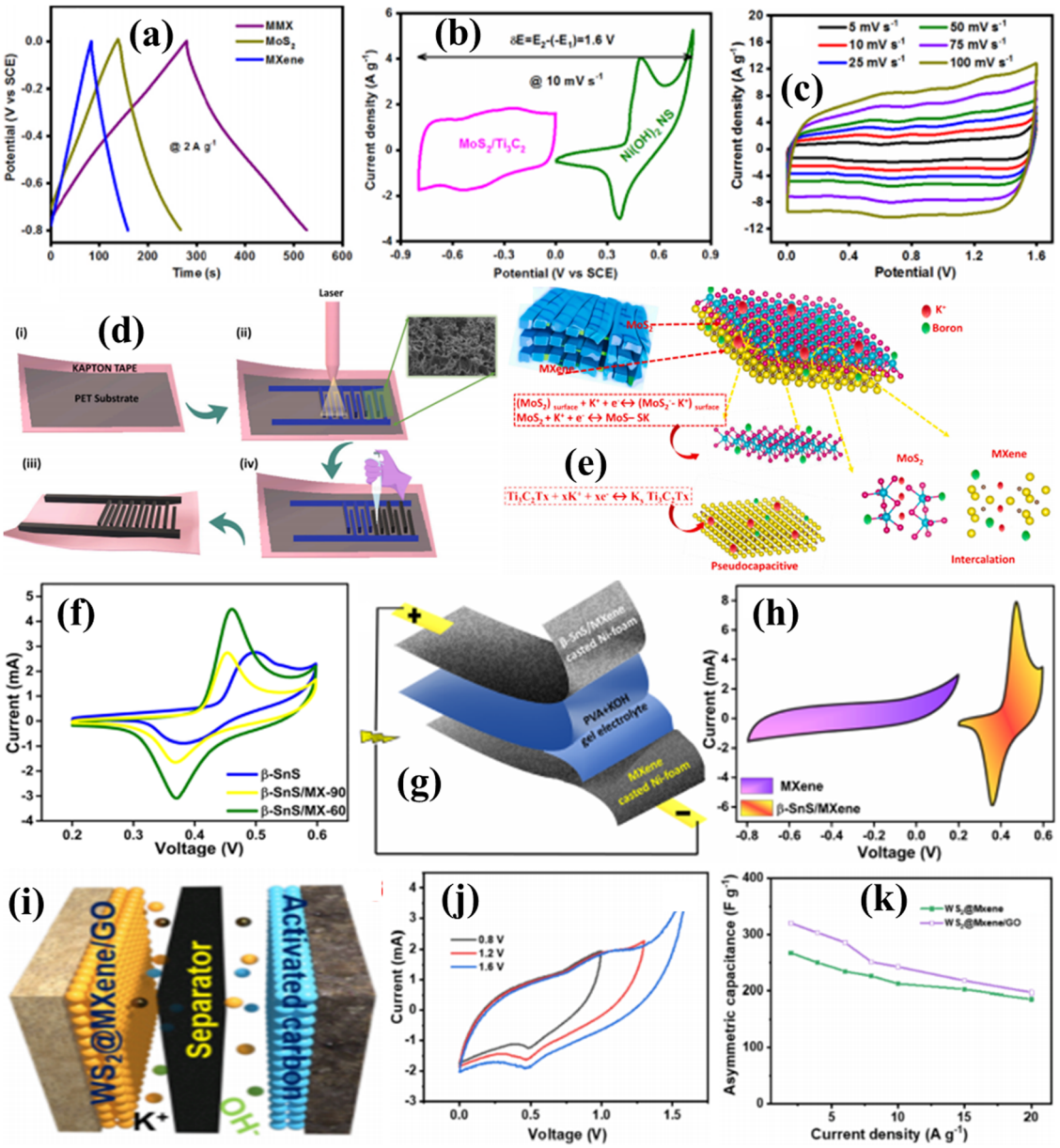

Fig. 9 (a) Comparative CD profile of MoS_2, MXene, and MoS_2@MXene. (b) CV curve showing the active potential window. (c) CV profile for MoS_2@MXene//$Ni(OH)_2$ device.[84] (d) Schematic of micro-SC fabrication. (e) Charge storage mechanism in the boron-modified 1T-MoS_2@MXene hybrid during electrochemical reactions.[60] (f) CV comparison of the β-SnS@MXene composite with β-SnS. (g) Schematic of the β-SnS@MXene//MXene device. (h) CV curve showing the active potential window of the device.[57] (i) Schematic of the WS_2@MXene@GO//AC device. (j) CV curves at different working potentials. (k) Specific capacitance comparison.[88]

into the WS_2@MXene composite further enhances the stability of the structure and its performance. Hussain *et al.*[88] prepared WS_2@MXene@GO nanocomposites in a 2D–2D heterostructure, which exhibited a specific capacitance of 1111 F g^{-1} at 2 A g^{-1} with excellent rate capability. The mass loading of the active material was maintained at 3 mg cm^{-2}. The WS_2@MXene@GO//AC device (Fig. 9i) demonstrated a specific energy of 114 W h kg^{-1} at 1010 W kg^{-1}, with 93.1% capacitance retention after 15 000 cycles. A similar CV at different potential windows confirmed the stability of the device, with a specific capacitance of 320 F g^{-1} (Fig. 9j and k).

4.2. MXene and transition-metal selenides

Transition-metal selenides commonly consist of metals combined with selenium. Selenium (Se), an element belonging to the oxygen group, has a lower electronegativity than both oxygen and sulfur. Because of its lower electronegativity, Se shows higher electrical conductivity, nearly on the order of 10^{-3} S m^{-1}. Transition-metal selenides and their composites are extensively studied for SC applications due to their properties, including high electrical conductivity and excellent chemical activity/stability. Selenides can be classified as either monometallic or bimetallic. Examples of selenides include

$NiSe_2$, $CoSe_2$, $MoSe_2$, VSe_2, WSe_2, $CrSe_2$, $SnSe_2$, $NiFe_2Se_4$, and $NiCo_2Se_4$.[63,91,92] Furthermore, forming composites of selenides with layered MXenes prevents agglomeration of selenides and increase the specific capacitance of the composite.

Nickel selenides ($NiSe_2$) exhibit good chemical activity and multiple oxidation states, making them suitable as SC electrode materials. However, their low cycle stability, rate capability, and conductivity hinder their application as electrode materials, which can be overcome by synthesizing suitable composite materials with MXene. $NiSe_2$@MXene, in a 2D–1D-type heterostructure configuration with 8 mg cm^{-2} mass loading, was reported by Jiang *et al.*[93] and exhibited a specific capacitance of 531.2 F g^{-1} at 1 A g^{-1}. The strong interaction in the composite is due to the wrapping of $NiSe_2$ crystals with ultrathin MXene. Vanadium diselenide (VSe_2) is a layered TMC containing a V layer sandwiched between two Se layers *via* van der Waals interactions. Due to the overlapping bands and interlayer gaps, VSe_2 possesses high electronic conductivity and chemical activity, which are helpful for energy storage applications. Further by synthesizing a heterostructure of VSe_2 with MXene, the limitation of damaging the sample due to agglomeration during cycling can be resolved. The VSe_2@MXene layered composite in a 2D–2D configuration, prepared *via* a hydrothermal method, showed a specific capacitance of 144 F g^{-1} at 1 A g^{-1} with 2 mg mass loading with 92.8% retention after 5000 charge–discharge cycles.[63] The enhanced states at the Fermi level, improved charge distribution, and lower ion diffusion barrier in the structure supported the improved charge storage performance (Fig. 10a–c). An electronic charge transfer occurs from the Ti 3d orbital of MXene to the V 3d orbital of VSe_2 due to the interaction between the layers. Moreover, the hybrid SC device VSe_2@MXene//MoS_2@MWCNT demonstrated an energy density of 42 W h kg^{-1} at a power density of 2316 W kg^{-1} with a 90% capacity retention after 5000 CD cycles. Furthermore, Siddu *et al.*[33] synthesized a ternary composite by adding CNT into the VSe_2@MXene, forming a 2D–2D/1D heterostructure with 1.2 mg mass loading, which showed superior energy storage performance. The VSe_2@MXene@CNT (Fig. 10d) provided structural stability and a specific capacitance of 151 F g^{-1}. The CD comparison profile shown in Fig. 10e indicates a longer discharge time for the composite material compared to the pristine materials. Furthermore, due to the addition of MXene and CNT into the structure, the capacitive nature of charge storage is the dominant contribution (77.6% at high scan rates) in the composite (Fig. 10f). The hybrid device VSe_2@MXene@CNT//MoS_2@MXene exhibited an energy density of 35.91 W h kg^{-1} at a power density of 1280 W kg^{-1}, with 99% capacity retention after 5000 cycles. $MoSe_2$ exhibits outstanding electrochemical activity and a high hypothetical capacitance for SC applications. The $MoSe_2$@MXene hybrid composite (2D–2D-type heterostructure), synthesized by Arulkumar *et al.*,[94] demonstrated a high specific capacitance of 1531.2 F g^{-1} at 1 A g^{-1}, where mass loading was 1.5 mg cm^{-2}. There is an increase in electrical conductivity, charge transfer rate, and active sites in the composite compared to the pristine samples. Similarly, the $MoSe_2$@MXene hybrid materials (2D–3D-type heterostructure), prepared by Chen *et al.*,[91] showed a specific capacitance of 1358.5 F g^{-1} at 1 A g^{-1} and 2.6 mg cm^{-2} mass loading. The capacitance of the composite was higher than that of $MoSe_2$ and MXene, as confirmed by the CV profile comparison shown in Fig. 10g. Further EIS analysis (Fig. 10h) confirmed a lower charge-transfer resistance (1.46 Ω) for the composite compared to the pristine materials. In addition, the hybrid device $MoSe_2$@MXene//AC showed a similar CV profile in a 1.6 V potential window (Fig. 10i) and exhibited an energy density of 55.6 W h kg^{-1} at a power density of 800.3 W kg^{-1}, with 94.1% capacitance retention after 10 000 cycles at a high current of 5 A g^{-1}. Hussain *et al.*[95] synthesized a symmetric device using the $MoSe_2$@MXene composite material (2D–2D-type heterostructure), which delivered a capacitance of 350 F g^{-1} with 93% capacitance retention after 5000 cycles, and a specific energy of 48 W h kg^{-1} at a specific power of 500 W kg^{-1}. Hence, the MXene composite supports the highly active $MoSe_2$ and enhances the active surface area and porosity. $CrSe_2$ consists of covalently bonded Se–Cr–Se monolayers, which are weakly bound together *via* the van der Waals forces. The structure shows strong Cr–Cr in-plane and Se–Se interlayer interactions. The intrinsic physical and electrical properties make it a suitable candidate for energy storage applications. $CrSe_2$@MXene, in a 2D–2D-type heterostructure, was prepared and studied for an all-solid-state symmetric supercapacitor (ASSS),[62] where the composite electrode, prepared with a 1 mg cm^{-2} mass loading, showed a maximum areal capacitance of 133 mF cm^{-2} at 2 mA cm^{-2} (Fig. 10j). Furthermore, the ASSS device (Fig. 10k) exhibited a maximum energy density of 7.11 mW h cm^{-2} at a power density of 355 mW cm^{-2}, retaining 82% of its capacitance after 5000 CD cycles (Fig. 10l). Additionally, WSe_2@MXene hybrid materials in a 2D–1D type heterostructure were prepared, showing improved interfacial interactions and conductivities.[96] The electrode achieved a specific capacitance of 840 F g^{-1} at 2 A g^{-1}. The fabricated symmetric device using eWSe_2@MXene exhibited a capacitance of 246 F g^{-1} at 2 A g^{-1}. Therefore, transition-metal selenides generally exhibit poor capacity retention, but the hybrid structures with MXene act as a reservoir for electrolytes, enhancing electrochemical activity and making the structure suitable for energy storage applications.

4.3. MXene and transition-metal tellurides

Tellurium (Te) is a solid material at room temperature and a semiconductor. Te shows higher electrical conductivity than sulfur, which has led its recent focus in energy storage applications. Metal sulfides and selenides are extensively studied for SC applications, whereas tellurides are less explored among TMCs. Since research on Te is still in its early stages, fewer articles have been reported, and we discussed some of them in this section. The high electrical conductivity, large atomic size, and low electronegativity of Te make tellurides suitable for energy storage applications. CoTe and NiTe have been reported for energy storage applications, where CoTe exhibited an energy density of 43.84 W h kg^{-1} at a power density of 738.88 W kg^{-1}, and NiTe showed a specific capacitance of 807 F g^{-1}.[97,98] The Co-doped NiTe electrode showed a specific capacitance of 1645.6 F g^{-1} at 1 A g^{-1}. The fabricated Co-doped NiTe//AC

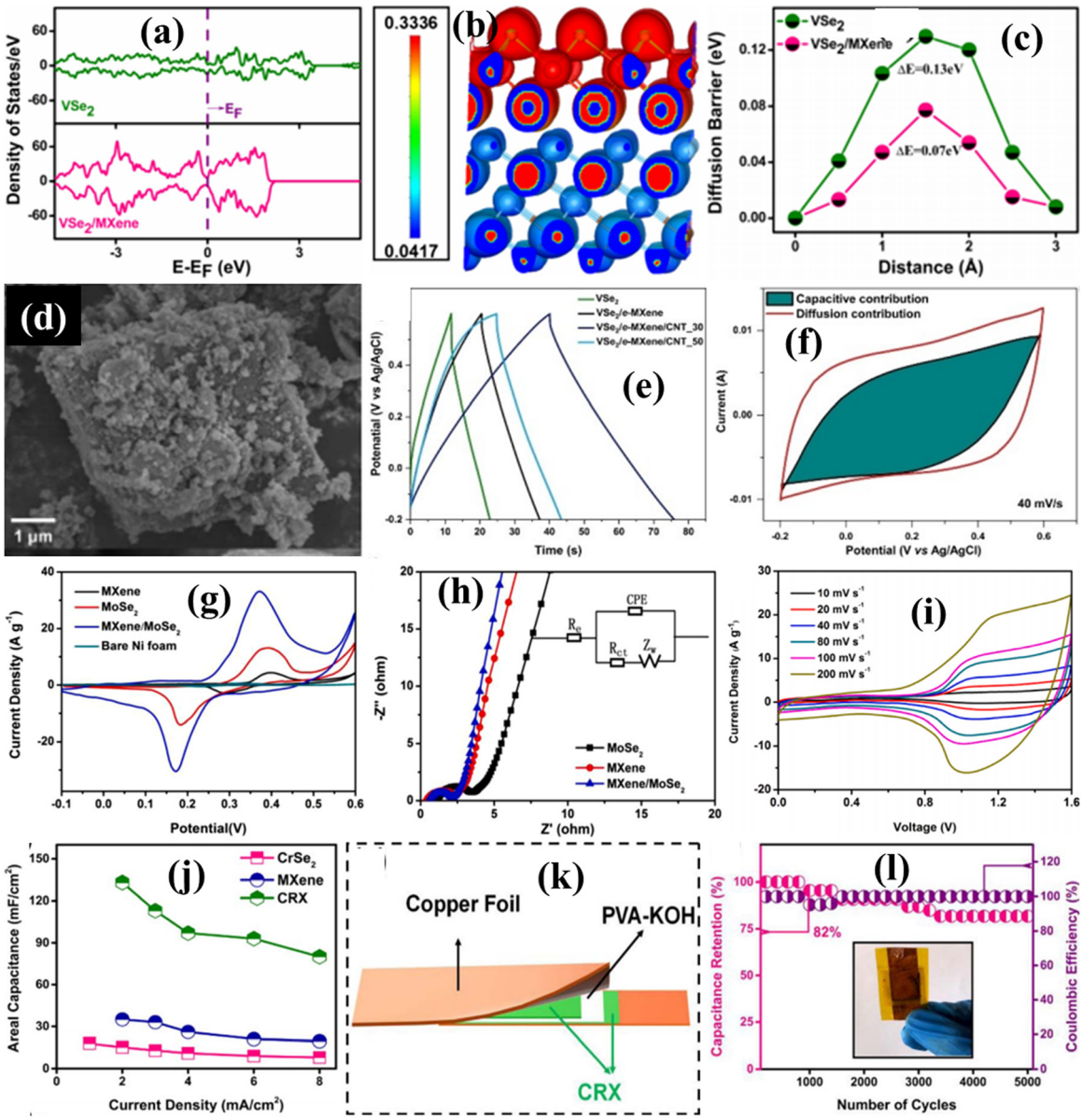

Fig. 10 (a) Density of states plot for VSe_2 and VSe_2@MXene, (b) charge density difference between VSe_2@MXene and VSe_2 (VSe_2 in red and the charge-losing MXene in blue), and (c) diffusion barrier plot comparing VSe_2 and VSe_2@MXene for positive electrolyte ions.[63] (d) SEM image of VSe_2@MXene@CNT, (e) comparison of the CD profile of the pristine samples with the VSe_2@MXene@CNT composite, and (f) CV curves showing the charge-storage contributions.[33] (g) CV comparison, (h) Nyquist plot of $MoSe_2$@MXene with MXene and $MoSe_2$ (inset shows the fitted equivalent circuit), and (i) CV profile of the device at different scan rates.[91] (j) Rate capability comparison of CrSe2@MXene, (k) schematic of the ASSS device, and (l) cycle stability and coulombic efficiency of the device (inset depicts the photographic image of device).[62]

device displayed a capacitance of 103.4 F g^{-1} and maintained 95% capacitance retention for 5000 CD cycles, with an energy density of 36.8 W h kg^{-1}.[99]

Furthermore, the unique properties of Te and its composites with MXene provide high electrolyte accommodation in the hybrid electrode, improving electrochemical performance. Vanadium telluride (VTe_2) is metallic and shows better electrochemical activity. VTe_2 has stronger interlayer coupling than other chalcogens, which makes it suitable for creating heterostructures that enhance the energy storage activity. VTe_2@MXene heterostructure, in a 2D–2D configuration, was synthesized through a hydrothermal process, where the VTe_2 nanosheet grown vertically on the MXene surface was confirmed by FESEM (Fig. 11a).[64] The composite delivered a specific capacitance of 250 F g^{-1} with a mass loading of 1 mg cm^{-2}, showing high cycle stability compared to the pristine samples (Fig. 11b). Computation studies confirmed an enhanced density of states near the Fermi level in the VTe_2@MXene due to the interaction with the MXene layers (Fig. 11c). Furthermore, density functional theory calculations showed improvement in the electronic Te 5p states near the Fermi level due to the presence of MXene, leading to improved performance of the VTe_2@MXene

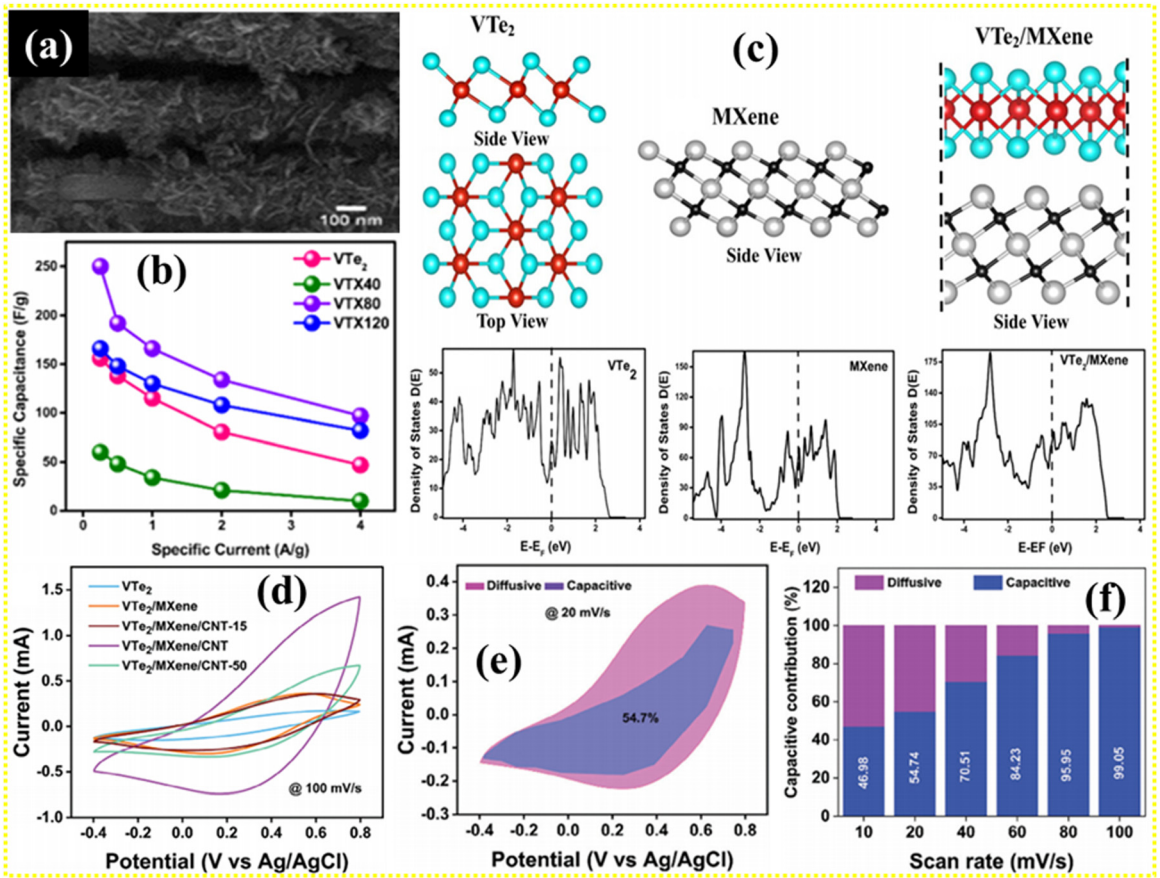

Fig. 11 (a) FESEM image of VTe_2@MXene, (b) rate capability profile for VTe_2 and VTe_2@MXene, and (c) optimized structures and total DOS for VTe_2, MXene, and VTe_2@MXene (vanadium, tellurium, titanium, and carbon atoms are denoted by red, sky blue, grey, and black spheres).[64] (d) CV profile comparison of VTe_2, VTe_2@MXene, and VTe_2@MXene@CNT, and (e) and (f) capacitive and diffusive contributions to charge storage in VTe_2@MXene@CNT.[32]

for SC applications. Consequently, the fabricated device, VTe_2@MXene//MoS_2@MXene, exhibited excellent performance with an energy density of 46.3 W h kg^{-1}, a maximum power density of 6400 W kg^{-1}, and 87% cycle stability after 7000 cycles.[64] Radhakrishnan *et al.* synthesized a VTe_2@MXene@CNT composite material in a 2D–2D/1D-type heterostructure for micro-SCs.[32] In this ternary composite, MXene and CNT avoided the restacking of VTe_2 and simultaneously enhanced its electrochemical activity. The comparative CV profile in Fig. 11d confirms the enhanced specific capacitance for VTe_2@MXene@CNT *i.e.* 136 mF cm^{-2} at 0.03 mA cm^{-2}. Additionally, the composite showed a rise in capacitive contribution from 45% (at 10 mV s^{-1}) to 99% (100 mV s^{-1}), as shown in Fig. 11e and f. Hence, MXene and CNT enhance charge adsorption, thereby increasing the capacitive contributions. Furthermore, the fabricated micro-SC showed an energy density of 6.84 μW h cm^{-2} and a power density of 304.7 μW cm^{-2}, with 78% retention in capacitance after 10 000 cycles. The device also showed stable CV characteristics even after bending, demonstrating its potential application in flexible electronics. The $CoTe_2$@MXene and ZnTe@MXene heterostructures (2D–3D type) were synthesized by Pan *et al.*[100] and exhibited specific capacities of 193.4 and 184 mA h g^{-1}, respectively, for K-ion storage. However, the capacities reduced to 62.2 and 64.7 mA h g^{-1} after 1000 cycles for $CoTe_2$@MXene and ZnTe@MXene, respectively. CoTe@MXene was also used as a catalyst separator to enhance the conversion of polysulfide in Li–S batteries. The mass loading of active materials was maintained at 1.2–1.8 mg cm^{-2} in this study.[101] This also improved the thermal durability of the separator while accelerating Li_2S nucleation and decomposition. The Li–S batteries fabricated using CoTe@MXene as separators exhibited a capacity of 1664 mA h g^{-1} with high cycle stability. Kamat *et al.*[102] synthesized $MoTe_2$@MXene *via* a modified hydrothermal route, and the composite displayed a reversible specific discharge capacity of 566 mA h g^{-1} at 0.1C and retained 71% of its initial capacity during rate performance. The composite material enhances Li-ion exposure and sustains structural stability for better performance. The discussion concludes with the potential applications of tellurides and MXene for energy storage applications. Furthermore, other metal tellurides in MXene-based composites can be explored for SC applications.

4.4. MXene and bimetallic chalcogenides

Bimetallic TMCs have gained attention due to their higher electrochemical activity, which results from the presence of two metals in their structure.[103] Additionally, the chemical activity arising from the multi-oxidation states of some metal

ions contributes to stable and efficient cycle stability. These bimetallic TMCs also experience less rate capabilities and volume expansion during the chemical process. Hence, synthesizing suitable heterostructure with MXene can enhance capacitance retention and maintain a stable structure to minimize volume expansion. Patra *et al.* used MXene as a template to synthesize $MoWS_2$ (MWS) nanosheets (2D–2D-type heterostructure), where the composite exhibited high chemical activity, as confirmed by the comparative CV profile (Fig. 12a).[70] The specific capacitance of 259 F g^{-1} was achieved at 0.2 A g^{-1} with an active mass loading of 1 mg cm^{-2}. Furthermore, the hybrid device $MoWS_2$@MXene//$CoSe_2$@CNT@rGO exhibited an energy density of 14 W h kg^{-1} at a specific power of 8000 W kg^{-1}, with 93% capacitance retention after 6000 cycles. The device showed capacitive- and diffusion-controlled contributions of 92% and 8%, respectively, at 60 mV s^{-1} (Fig. 12b and c). Li *et al.* have reported a 1T-$Mo_{0.71}W_{0.29}S_2$@MXene heterostructure (2D–2D-type heterostructure) with a specific capacitance of 284 F g^{-1} at 1 A g^{-1}.[71]

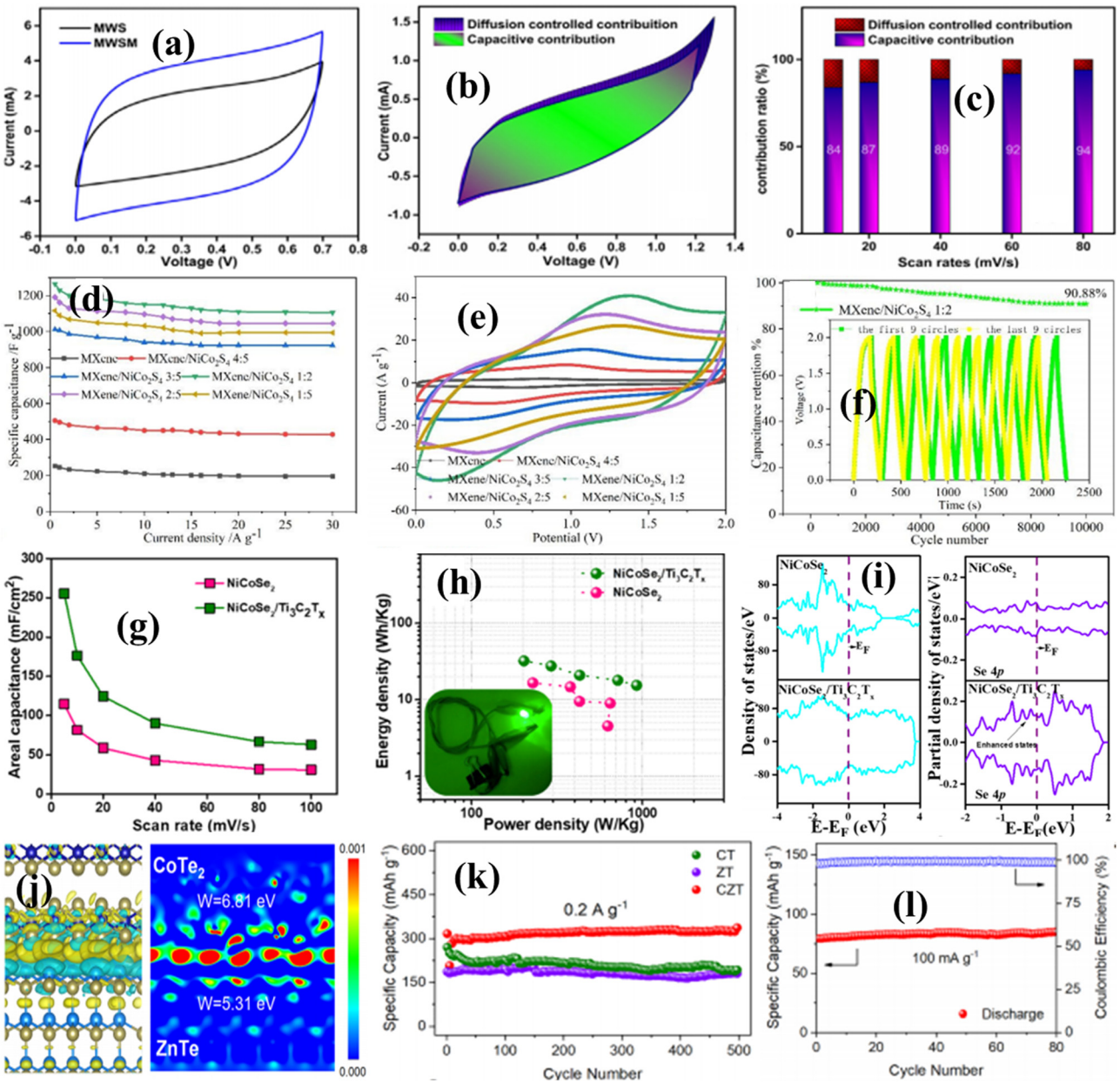

Fig. 12 (a) Comparative CV profiles of $MoWS_2$ and $MoWS_2$@MXene, (b) charge storage contributions at 60 mV s^{-1}, and (c) bar diagram of charge storage contributions at different scan rates.[70] (d) Rate capability comparison of $NiCo_2S_4$@MXene samples, (e) CV comparison of a device fabricated using the $NiCo_2S_4$@MXene samples, where AC was used as the negative material, and (f) cycle stability of the optimized $NiCo_2S_4$@MXene//AC device.[72] (g) Rate capability of $NiCoSe_4$@MXene, (h) Ragone plot of $NiCoSe_4$@MXene//AC device with inset showing the LED test and (i) TDOS plot and PDOS for Se 4p for $NiCoSe_2$ and $NiCoSe_2$@MXene composite.[61] (j) charge density difference and work function of CoTe2@ZnTe, (k) cycle performance of CoTe2@ZnTe@MXene for 500 cycles, and (l) specific capacity of the device for 80 cycles.[100]

The composite shows high structural stability resulting from the combined effect of strain caused by W doping and *in situ* growth on MXene. Furthermore, the constructed symmetric SC device showed excellent electrochemical performance, which is tabulated in Table 1.

Furthermore, Patra *et al.*[59] introduced boron carbon nitride to the $MoWS_2$@MXene composite (2D–2D-type heterostructure) to form a ternary composite, $MoWS_2$@BCN@MXene, for enhanced capacitance. The ternary composite was used to fabricate a solid-state symmetric device, which showed a specific capacitance of 289 mF cm^{-2} at 0.6 mA cm^{-2}, with 91% capacitance retention over 5000 cycles at 10 mA cm^{-2}. The calculated quantum capacitance was improved and correlated with the observed capacitance. Furthermore, the charge transfer from the Mo 4d orbital of $MoWS_2$ and C 2p orbital of BCN to the C 2p orbital of MXene was analyzed through computational calculations, confirming the improvement in the charge kinetics of the ternary composite. A 3D hybrid composite of $NiCo_2S_4$@MXene (2D–3D-type heterostructure) was prepared and optimized for a high specific capacitance of 1266 F g^{-1} at 0.5 A g^{-1}, with 95% capacitance retention after 10 000 cycles.[72] The specific capacitance comparison at different current densities for composites synthesized with different material mass ratios is depicted in Fig. 12d. Asymmetric SC devices of all the composites were separately fabricated, where AC was used as the negative electrode material. The device with a 1 : 2 mass ratio of electrodes showed a high specific capacitance of 621 F g^{-1}, as confirmed by the comparative CV profile (Fig. 12e), and maintained 90.88% capacitance retention over 10 000 cycles at 5 A g^{-1} (Fig. 12f). The device exhibited an energy density of 72.82 W h kg^{-1} at a power density of 0.635 kW kg^{-1}. Pathak *et al.*[106] separately used $NiCo_2S_4$ and MXenes as the positive and negative electrodes, respectively, for the fabrication of an asymmetric SC device that delivered areal and gravimetric energy densities of 14.86 mW h cm^{-2} and 14.86 W h kg^{-1}, respectively. The same research group synthesized the $NiCo_2S_4$@MXene composite (2D–3D/0D-type heterostructure), which delivered a specific capacitance of 1076 F g^{-1} with 80% capacitance retention over 5000 cycles. Active mass loading of 1 mg cm^{-2} was used for this study.[31] An asymmetric device, $NiCo_2S_4$@MXene//MXene, was fabricated that exhibited an energy density of 11.5 μW h cm^{-2} with 80% capacitance retention and showed good stability after bending at various angles. Again, $NiCo_2S_4$ was anchored on nanocarbon (rGO@MWCNT), and $NiCo_2S_4$@rGO@MWCNT//MXene device performance was observed to be lower than the $NiCo_2S_4$@MXene//MXene composite. By contrast, the device with nanocarbon showed high capacitance retention due to the presence of carbon materials. Similarly, Pathak *et al.* prepared $MnCo_2S_4$@MXene and $NiCo_2S_4$@MXene (2D–3D-type heterostructure) on the carbon-cloth electrode *via* a hydrothermal synthesis process, which exhibited areal capacitances of 274 and 206 mF cm^{-2} at a current density of 0.6 mA cm^{-2}, respectively.[104] The $MnCo_2S_4$@MXene//AC solid-state flexible device exhibited a maximum areal energy density of 20 μW h cm^{-2} at 750 mW cm^{-2} compared to the $NiCo_2S_4$@MXene//AC device. $NiCoSe_2$@MXene (2D–2D-type heterostructure) was prepared by Samal *et al.*,[61] where the dual metal presence and unique morphology showed excellent charge-storage performance. The $NiCoSe_2$@MXene//MXene device demonstrates a specific capacitance of 254.10 mF cm^{-2} at 5 mV s^{-1} (Fig. 12g) with an energy density of 32.05 W h kg^{-1} at a power density of 0.2 kW kg^{-1} and maintains 15.39 W h kg^{-1} of energy density at a power density of 0.92 kW kg^{-1} (Fig. 12h). The computational study confirmed that charge transfer from MXene to $NiCoSe_2$ enhances the electronic states at the Fermi energy, thereby improving the chemical activity for high charge storage (Fig. 12i). Patel *et al.*[105] synthesized the Co-$NiSe_2$@MXene composite (in 2D–1D-type heterostructure), where the nanorod-like Co-$NiSe_2$ wrapped around MXene, exhibiting a specific capacitance of 1394.8 F g^{-1} at 1 A g^{-1} with 67% capacitance retention over 5000 cycles at 20 A g^{-1}. Furthermore, $Cu_{0.5}Co_{0.5}Se_2$ nanosheets were prepared by Dakka *et al.*[107] and used as positive electrodes in the $Cu_{0.5}Co_{0.5}Se_2$//MXene device. The device operated at a working potential of 1.6 V and delivered a high energy density of 84.17 W h kg^{-1} at 0.604 kW kg^{-1}, with 91% capacitance retention after 10 000 cycles. Dual transition metal tellurides ($CoTe_2$@ZnTe) are anchored on the MXene (2D–3D-type heterostructure) to form a composite structure proposed by Pan *et al.*,[100] where interface engineering regulates the electronic state and improves the K^+ kinetics in the composite (Fig. 12j). The composite delivered a specific capacity of 365.3 mA h g^{-1} at 0.1 A g^{-1}, which is higher than that of $CoTe_2$@MXene and ZnTe@Mxene. The material maintained a capacity of 339.1 mA h g^{-1} after 500 cycles (Fig. 12k), with a mass loading of active material ranging from 1.2 to 1.8 mg cm^{-2}. Furthermore, the full-cell device using $CoTe_2$@ZnTe@MXene and Prussian blue potassium as anodes and cathodes showed a specific capacity of 85 mA h g^{-1} at 0.1 A g^{-1} and maintained 93% of its capacity after 400 charge–discharge cycles (Fig. 12l). Li *et al.*[108] studied the $Co_{0.5}Ni_{0.5}Te_2$-grafted MXene heterostructure (2D–3D-type heterostructure), which enhanced the sulfur redox kinetics in Li–S batteries. The heterostructure exhibited high polar active sites that enhanced the chemical adsorption of polysulfides and provided an accelerated pump for rapid Li^+ diffusion, as observed in performance analysis, theoretical calculations, and *in situ* Raman spectroscopy. Table 1 shows the detailed electrochemical performance of the TMC@MXene structures.

5. Summary, challenges, and future perspectives

Recently, SCs have gained attention because of their promising performance and possible uses in electronic gadgets and flexible devices. SCs offer higher power density, fast charge kinetics, and longer life cycles than batteries. However, the lower energy density of SC hinders their practical applications. Hence, different strategies such as surface modification, functionalization, composite materials synthesis, and hetero-material doping have been adapted to synthesize new hybrid electrode materials. TMCs are a class of materials basically

Table 1 Detailed electrochemical charge storage performance of different TMC@Mxene structure-based electrodes and their device performance. Energy density: ED, power density: PD, and activated carbon: AC

		Electrode performance			Device performance				
Sl. No	Ref.	Material	Capacitance (F g^{-1}) or capacity (C g^{-1} or mA h g^{-1})	Cycle stability	Device	Capacitance (F g^{-1}) or capacity (C g^{-1} or mA h g^{-1}), Potential (V)	Max. ED at Min. PD	Max. PD at Min. ED	Cycle stability
MXene-transition metal sulfides									
1	58	1T VS_2@$Ti_3C_2T_x$	106.38 F g^{-1} at 0.2 A g^{-1}	—	1T VS_2@$Ti_3C_2T_x$// $Ti_3C_2T_x$	115 F g^{-1} at 0.8 A g^{-1}, 1.6	41.13 W h kg^{-1} at 793.5 W kg^{-1}	11 169.72 W kg^{-1} at 22.96 W h kg^{-1}	85% over 5000 cycles at 30 A g^{-1}
2	75	VS_2@$Ti_3C_2T_x$	1791.4 F g^{-1} (895.7 C g^{-1}) at 1 A g^{-1}	90.6% over 10 000 cycles at 5 A g^{-1}	VS_2@$Ti_3C_2T_x$// Fe_3O_4@rGO	228.4 F g^{-1} (365.4 C g^{-1}) at 1 A g^{-1}, 1.6	73.9 W h kg^{-1} at 728.2 W kg^{-1}	7273.7 W kg^{-1} at 52.9 W h kg^{-1}	97.7% over 10 000 cycles at 8 A g^{-1}
3	77	1T VS_2@ $Ti_3C_2T_x$@CNT	505.05 F g^{-1} at 0.2 A g^{-1}	84.3% over 5000 cycles at 5 A g^{-1}	1T VS_2@$Ti_3C_2T_x$@CNT// CNT	149.55 F g^{-1} at 2 A g^{-1}, 1.7	59.85 W h kg^{-1} at 7303.72 W kg^{-1}	96 908.1 W kg^{-1} at 9.96 W h kg^{-1}	93% over 5000 cycles at 15 A g^{-1}
4	76	VS_2@Ti_3C_2	191.3 mA h g^{-1} at 1 A g^{-1}	91.6% over 5000 cycles at 2 A g^{-1}	VS_2@Ti_3C_2//Ti_3C_2	88.1 F g^{-1} at 1 A g^{-1}, 1.4	24 W h kg^{-1} at 1288 W kg^{-1}	—	82.2% over 5000 cycles at 2 A g^{-1}
5	79	CoS_2@MXene	1320 F g^{-1} at 1 A g^{-1}	83.6% over 3000 cycles at 10 A g^{-1}	CoS_2@MXene//rGO	80.6 F g^{-1} at 1 A g^{-1}, 1.6	28 W h kg^{-1} at 800 W kg^{-1}	—	98% over 5000 cycles at 5 A g^{-1}
6	82	NiS@Ti_3C_2	840.4 C g^{-1} at 1 A g^{-1}	66.5% over 5000 cycles at 10 A g^{-1}	NiS@Ti_3C_2//Ti_3C_2	69.4 C g^{-1} at 0.5 A g^{-1}, 1.9	20 W h kg^{-1} at 500 W kg^{-1}	10 000 W kg^{-1} at 5.1 W h kg^{-1}	71.4% over 10 000 cycles at 2 A g^{-1}
7	81	NiS@$Ti_3C_2T_x$	554.1 mA h g^{-1} (857.8 F g^{-1}) at 1 A g^{-1}	99.49% over 3000 cycles at 5 A g^{-1}	NiS@$Ti_3C_2T_x$// Graphene@AC	56.73 F g^{-1} at 1 A g^{-1}, 1.5	17.688 W h kg^{-1} at 750 W kg^{-1}	—	97.7% over 3000 cycles at 10 A g^{-1}
8	83	$N_{i3}S_2$@Ti_3C_2	2204 F g^{-1} at 1 A g^{-1}	76.3% over 5000 cycles at 10 A g^{-1}	$N_{i3}S_2$@Ti_3C_2//AC	66.5 F g^{-1} at 0.5 A g^{-1}, 1.6	23.6 W h kg^{-1} at 399.2 W kg^{-1}	4004.4 W kg^{-1} at 10 W h kg^{-1}	96.7% over 5000 cycles at 1 A g^{-1}
9	80	CuS@Ti_3C_2	169.5 C g^{-1} at 1 A g^{-1}	90.5% over 5000 cycles at 5 A g^{-1}	CuS@Ti_3C_2//Ti_3C_2	49.3 F g^{-1} at 1 A g^{-1}, 1.5	15.4 W h kg^{-1} at 750.2 W kg^{-1}	—	82.4% over 5000 cycles at 2 A g^{-1}
10	84	MoS_2@MXene	583 F g^{-1} at 5 A g^{-1}	96.5% over 5000 cycles at 5 A g^{-1}	MoS_2@MXene// $Ni(OH)_2$	153 F g^{-1} at 1 A g^{-1}, 1.6	54 W h kg^{-1} at 860 W kg^{-1}	—	90% over 10 000 cycles at 5 A g^{-1}
11	85	MoS_2@Ti_3C_2	342 F g^{-1} at 0.4 A g^{-1}	99% over 10 000 cycles at 20 A g^{-1}	—	—	—	—	—
12	86	2H-MoS_2@$Ti_3C_2T_x$	303.8 F g^{-1} at 1 A g^{-1}	82% over 10 000 cycles at 10 A g^{-1}	2H-MoS_2@$Ti_3C_2T_x$// 2H-MoS_2@$Ti_3C_2T_x$	115.2 F g^{-1} at 0.5 A g^{-1}, 0.6	5.1 W h kg^{-1} at 298 W kg^{-1}	2983 W kg^{-1} at 2.9 W h kg^{-1}	72.3% over 10 000 cycles at 5 A g^{-1}
13	87	MoS_2@$Ti_3C_2T_x$	439 F g^{-1} at 5 mV s^{-1}	96% over 10 000 cycles at 20 A g^{-1}	MoS_2@$Ti_3C_2T_x$// MoS_2@$Ti_3C_2T_x$	—	13.1 W h kg^{-1} at 300 W kg^{-1}	30 000 W kg^{-1} at 6.3 W h kg^{-1}	91% over 10 000 cycles at 20 A g^{-1}
14	60	B-modifiedMoS_2@ $Ti_3C_2T_x$	420 F g^{-1} at 1 A g^{-1}	—	Symmetric micro SC	72.31 mF cm^{-2} at 0.075 mA cm^{-2}, 0.8	5.7 μW h cm^{-2} at 77 μW cm^{-2}	—	100% over 10 000 cycles at 0.025 mA cm^{-2}
15	57	SnS@$Ti_3C_2T_x$	615 mF cm^{-2} at 4 mA cm^{-2}	—	SnS@$Ti_3C_2T_x$//$Ti_3C_2T_x$	109 mF cm^{-2} at 6 mA cm^{-2}, 1.5	34.06 μW h cm^{-2} at 6.2 mW cm^{-2}	—	81% over 6000 cycles
16	90	WS_2@$Ti_3C_2T_x$	373 F g^{-1} at 0.4 A g^{-1}	91.2% over 1000 cycles at 2 A g^{-1}	—	—	—	—	—

Table 1 (*continued*)

Sl. No	Ref.	Electrode performance: Material	Capacitance ($F\ g^{-1}$) or capacity ($C\ g^{-1}$ or $mA\ h\ g^{-1}$)	Cycle stability	Device performance: Device	Capacitance ($F\ g^{-1}$) or capacity ($C\ g^{-1}$ or $mA\ h\ g^{-1}$), Potential (V)	Max. ED at Min. PD	Max. PD at Min. ED	Cycle stability
17	88	WS_2@MXene@GO	1111 F g^{-1} at 2 A g^{-1}	97.15% over 5000 cycles at 10 A g^{-1}	WS_2@MXene@GO//AC	320 F g^{-1} at 2 A g^{-1}, 1.6	114 W h kg^{-1} at 1010 W kg^{-1}	10 820 W kg^{-1} at 70 W h kg^{-1}	93.1% over 15 000 cycles at 10 A g^{-1}
MXene-transition metal selenides									
18	93	$NiSe_2$@$Ti_3C_2T_x$	531.2 F g^{-1} at 1 A g^{-1}	—	—	—	—	—	—
19	63	1T-VSe_2@$Ti_3C_2T_x$	144 F g^{e1} at 1 A g^{-1}	92.8% over 5000 cycles at 6 A g^{-1}	1T-VSe_2@$Ti_3C_2T_x$// MoS_2@MWCNT	—, 1.65	42 W h kg^{-1} at 2316 W kg^{-1}	—	90% over 5000 cycles at 8 A g^{-1}
20	33	VSe_2@$Ti_3C_2T_x$@ CNT	151 F g^{-1} at 1 mA	98.1% over 5000 cycles at 8 A g^{-1}	VSe_2@$Ti_3C_2T_x$@CNT// MoS_2@$Ti_3C_2T_x$	101 F g^{-1} at 1.6 A g^{-1}, 1.5	35.91 W h kg^{-1} at 1280 W kg^{-1}	6350 W kg^{-1} at 24.14 W h kg^{-1}	99.1% over 5000 cycles at 8 A g^{-1}
21	94	$MoSe_2$@$Ti_3C_2T_x$	1531.2 F g^{-1} at 1 A g^{-1}	96.3% over 10 000 cycles at 10 A g^{-1}	$MoSe_2$@$Ti_3C_2T_x$//AC	234.23 F g^{-1} at 1 A g^{-1}, 1.8	58.8 W h kg^{-1} at 800.3 W kg^{-1}	—	94.1% over 10 000 cycles at 20 A g^{-1}
22	91	$MoSe_2$@$Ti_3C_2T_x$	1358.5 F g^{-1} at 1 A g^{-1}	96.3% over 10 000 cycles at 10 A g^{-1}	$MoSe_2$@$Ti_3C_2T_x$//AC	156.3 F g^{-1} at 1 A g^{-1}, 1.6	55.6 W h kg^{-1} at 800.3 W kg^{-1}	16 086.9 W kg^{-1} at 36.2 W h kg^{-1}	94.1% over 10 000 cycles at 5 A g^{-1}
23	95	$MoSe_2$@Ti_3C_2	—	—	$MoSe_2$@Ti_3C_2// $MoSe_2$@Ti_3C_2	350 F g^{-1} at 1 A g^{-1}, 1.0	48 W h kg^{-1} at 500 W kg^{-1}	10 000 W kg^{-1} at 30 W h kg^{-1}	89% over 5000 cycles at 10 A g^{-1}
24	62	$CrSe_2$@Ti_3C_2	133 mF cm^{-2} at 2 mA cm^{-2}	81.25% over 5000 cycles at 10 mA cm^{-2}	$CrSe_2$@Ti_3C_2// $CrSe_2$@Ti_3C_2	80 mF cm^{-2} at 0.8 mA cm^{-2}, 0.8	7.11 μW h cm^{-2} at 355 μW cm^{-2}	2000 μW cm^{-2} at 1.11 μW h cm^{-2}	82% over 5000 cycles at 6 mA cm^{-2}
25	96	WSe_2@MXene	840 F g^{-1} at 2 A g^{-1}	92% over 5000 cycles at 10 A g^{-1}	WSe_2@MXene// WSe_2@MXene	246 F g^{-1} at 2 A g^{-1}, 0.6	12 W h kg^{-1} at 600 W kg^{-1}	300 W kg^{-1} at 5.7 W h kg^{-1}	90% over 5000 cycles at 5 A g^{-1}
MXene-transition metal tellurides									
26	64	VTe_2@MXene	250 F g^{-1} at 0.25 A g^{-1}	83.5% over 7000 cycles at 8 A g^{-1}	VTe_2@MXene// MoS_2@MXene	130 F g^{-1} at 0.5 A g^{-1}, 1.6	46.3 W h kg^{-1} at 400 W kg^{-1}	6400 W kg^{-1} at 16 W h kg^{-1}	87% over 7000 cycles at 8 A g^{-1}
27	32	VTe_2@MXene@ CNT	136 mF cm^{-2} at 0.03 mA cm^{-2}	—	Micro SC	34.2 mF cm^{-2} at 0.25 mA cm^{-2}, 1.2	6.84 μW h cm^{-2} at 304.7 μW cm^{-2}	—	78% over 10 000 cycles
Bimetallic chalcogenides and MXenes									
28	70	$MoWS_2$@MXene	259 F g^{-1} at 0.2 A g^{-1}	89% over 6000 cycles at 10 A g^{-1}	$MoWS_2$@MXene// $CoSe_2$@CNT@rGO	60 F g^{-1} at 7 A g^{-1}, 1.3	14 W h kg^{-1}	8000 W kg^{-1}	93% over 6000 cycles at 20 A g^{-1}
29	71	$MoWS_2$@MXene	284 F g^{-1} at 1 A g^{-1}	99.2% over 8000 cycles at 10 A g^{-1}	$MoWS_2$@$Ti_3C_2T_x$// $MoWS_2$@$Ti_3C_2T_x$	136 mF cm^{-2} at 1 mA cm^{-2}, 0.7	9.3 μW h cm^{-2} at 0.3 mW cm^{-2}	7.1 mW cm^{-2} at 3.9 μW h cm^{-2}	86.1% over 8000 cycles at 10 mA cm^{-2}
30	59	$MoWS_2$@BCN@ MXene	—	—	Symmetric device	289 mF cm^{-2} at 0.6 mA cm^{-2}, 0.7	19.73 μW h cm^{-2}	589.09 μW cm^{-2}	91% over 5000 cycles at 10 mA cm^{-2}
31	72	$NiCo_2S_4$@MXene	1266 F g^{-1} at 0.5 A g^{-1}	95.21% over 10 000 cycles at 5 A g^{-1}	$NiCo_2S_4$@MXene//AC	621 F g^{-1} at 0.5 A g^{-1}, 2.0	72.82 W h kg^{-1} at 635 W kg^{-1}	39 600 W kg^{-1} at 18.95 W h kg^{-1}	90.88% over 10 000 cycles at 5 A g^{-1}

Table 1 (*continued*)

Sl. No	Ref.	Electrode performance			Device performance				
		Material	Capacitance (F g^{-1}) or capacity (C g^{-1} or mA h g^{-1})	Cycle stability	Device	Capacitance (F g^{-1}) or capacity (C g^{-1} or mA h g^{-1}), Potential (V)	Max. ED at Min. PD	Max. PD at Min. ED	Cycle stability
32	31	$NiCo_2S_4$@MXene	1076 F g^{-1} at 3 A g^{-1}	80% over 5000 cycles at 3 A g^{-1}	$NiCo_2S_4$@MXene// MXene	57.47 mF cm^{-2} at 0.6 mA cm^{-2}, 1.2	11.5 μW h cm^{-2}	1.24 mW cm^{-2}	90% over 5000 cycles at 10 mA cm^{-2}
33	104	$NiCo_2S_4$@MXene	206 mF cm^{-2} at 0.6 mA cm^{-2}	—	$NiCo_2S_4$@MXene//AC	27.58 mF cm^{-2} at 0.1 mA cm^{-2}, 1	6.47 μW h cm^{-2} at 824 mW cm^{-2}	—	84% over 5000 cycles
34	104	$MnCo_2S_4$@MXene	274 mF cm^{-2} at 0.6 mA cm^{-2}	—	$MnCo_2S_4$@MXene//AC	63.3 mF cm^{-2} at 0.1 mA cm^{-2}, 1.3	20 μW h cm^{-2} at 750 mW cm^{-2}	1.24 mW cm^{-2}	80% over 5000 cycles
35	61	$NiCo_2Se_4$@MXene	—	—	$NiCo_2Se_4$@MXene// MXene	160.25 F g^{-1} at 0.5 A g^{-1}, 1.2	32.05 W h kg^{-1} at 200 W kg^{-1}	920 W kg^{-1} at 15.39 W h kg^{-1}	95.67% over 10 000 cycles at 10 A g^{-1}
36	105	$CoNiSe_2$@MXene	1394.8 F g^{-1} at 1 A g^{-1}	67% over 5000 cycles at 20 A g^{-1}	—	—	—	—	—
37	100	$CoTe_2$@ZnTe@MXene	365 mA h g^{-1} at 0.1 A g^{-1}	—	$CoTe_2$@ZnTe@MXene// Blue potassium	79.8 mA h g^{-1} at 0.1 A g^{-1}	220.2 W h kg^{-1} at 110.8 W kg^{-1}	827.2 W kg^{-1} at 113 W h kg^{-1}	93% over 400 cycles at 0.1 A g^{-1}

sulfides, selenides, and tellurides, emerging for energy storage applications due to their unique physical and electrochemical properties. Metal sulfides have been vastly studied, and tellurides have recently attracted interest for energy storage applications. Furthermore, to improve the energy storage properties of TMCs, carbon-based materials and MXene are used to form composites. Since the discovery of MXene in 2011, MXene ($Ti_3C_2T_x$) has gained immense attention for energy storage applications due to its redox sites and high ion adsorption sites, owing to its 2D structure. Therefore, MXene provides a larger surface area for charge adsorption, and its interlayer facilitates ion intercalation. Furthermore, by forming composites with TMCs, the restacking or structural damages of MXene can be reduced. Hence, TMC@MXene heterostructures are being explored for energy storage applications. In this review, different TMCs (sulfides, selenides, and tellurides) and MXene composites for SC are extensively discussed. The structural design, device fabrication, and electrochemical properties of several TMC@MXene are discussed. Furthermore, computational analyses of these composites have been carried out in several reports to study the mechanisms behind the charge storage process. To solve the problems associated with these composite materials for SC, further research is ongoing at a rapid pace. Key factors that need to be addressed for the practical utilization of these composite materials include material availability, production costs, device stability, chemical toxicity, device scalability, and environmental safety.

Although much research has been conducted on MXene and TMC composites, there are further challenges to address for better device fabrication and commercialization of SCs. MXenes have challenges like the scalability of the material, precursor availability, toxic synthesis routes, production costs, and stability. Furthermore, TMCs@MXene composites used in SC are limited because of less electronic conductivity, synthesis complexity, environmental sensitivity, restacking/agglomeration issues, cyclic instability, and limited insights into the characteristics of materials. The self-restacking and agglomeration of theses composites cause damage to the electrodes during cycles and further limit their application in flexible electrode fabrication. Hence, future ideas and systematic research should be conducted, as summarized below (Fig. 13):

• Theoretical work is helpful for understanding and reducing the experimental work for better electrode synthesis. Hence, computational studies are required for TMCs@MXene composites to enable the preparation of more chemically active electrodes, thereby reducing the time and cost of the research.

• Recently, new classes of MXenes, such as V_2CT_x, Nb_2CT_x, and $Nb_4C_3T_x$, have been explored. These materials provide different metal redox sites that need further analysis. Hence, hybrid materials based on these MXenes and TMCs need to be explored. Furthermore, heterostructure composites of monometallic and bimetallic TMCs ($NiCo_2S_4/MoS_2$, $CuCoS_4/WS_2$, and $CoNi_2Se_4/SnS_2$) could be explored.

• Tellurides have been less explored for energy storage applications. Hybrid materials combining tellurides and MXenes may emerge as promising candidates for energy storage. Materials such

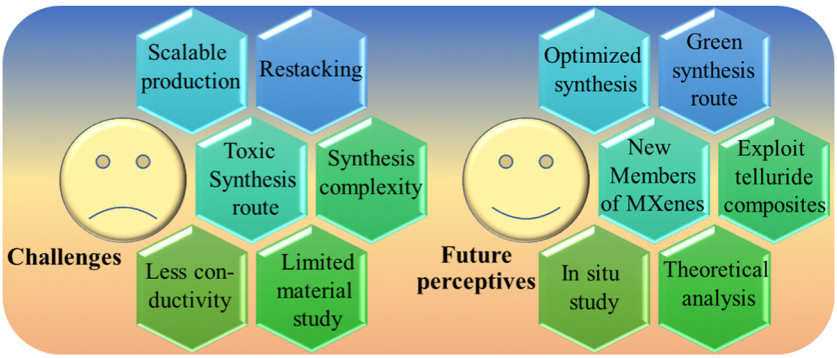

Fig. 13 Schematic depicting the challenges and future perspectives for TMCs@MXene composites for SC applications.

as Bi_2Te_3, GeTe, PbTe, Si_2Te_3, and $AgAuTe_4$ and their MXene-based hybrids could be explored for energy storage applications.

• TMCs@MXene composites contain both TMCs and MXenes, and the characteristics of both materials influence the charge-storage performance. So, both materials need to be optimized separately and in combination, focusing on factors such as metal concentration, synthesis time, stability, and synthesis process, to achieve better electrochemical performance.

• The MXene synthesis process is toxic because of the use of acids for etching. Furthermore, the synthesis of TMCs@MXene composites is a complex process. A green synthesis route should be developed for environmental safety, and acid-free electrodes would reduce unwanted reactions during the chemical process, which further improves the stability of the device.

• The energy densities of SCs made from the TMCs@MXene composites still need to be enhanced. Recently, metal-ion capacitors have been vastly studied, and the utilization of these composites in metal-ion hybrid capacitors needs to be further explored. Furthermore, other electrolytes (organic and gel type) should be considered to improve the overall performance of the device. Problems with the potential window, thermal stability, and safety of the device are mainly related to the electrolytes.

• To develop high-performance SCs, the reaction mechanism during the charge storage process needs to be understood. Hence, *in situ* TEM, XRD, RAMAN, and XPS, along with advanced characterization techniques, need to be studied and analyzed. This analysis will provide insights into the chemical reactions and facilitate the fabrication of environmentally safe devices.

Data availability

No primary research results, software, or code have been included, and no new data were generated or analyzed as part of this review.

Conflicts of interest

The authors declare no conflict of interest.

Acknowledgements

The authors extend their appreciation for the financial assistance provided by the SERB Core Research Grant (Grant No. CRG/2022/000897) and the Department of Science and Technology (DST/NM/NT/2019/205(G)). They also express gratitude for the support received through the Minor Research Project Grant from Jain University (JU/MRP/CNMS/29/2023). Gopinath Sahoo acknowledges the DST-SERB for the National Post-Doctoral Fellowship (Grant No. PDF/2023/000545).

References

1 J. Wang, V. Malgras, Y. Sugahara and Y. Yamauchi, *Nat. Commun.*, 2021, **12**, 3563.
2 K. Ge, H. Shao, P.-L. Taberna and P. Simon, *ACS Energy Lett.*, 2023, **8**, 2738–2745.
3 D. P. Chatterjee and A. K. Nandi, *J. Mater. Chem. A*, 2021, **9**, 15880–15918.
4 G. Sahoo, S. R. Polaki, S. Ghosh, N. G. Krishna, M. Kamruddin and K. Ostrikov, *Energy Storage Mater.*, 2018, **14**, 297–305.
5 K. Nasrin, V. Sudharshan, K. Subramani and M. Sathish, *Adv. Funct. Mater.*, 2022, **32**, 2110267.
6 Z. Lin, X. Li, H. Zhang, B. B. Xu, P. Wasnik, H. Li, M. V. Singh, Y. Ma, T. Li and Z. Guo, *Inorg. Chem. Front.*, 2023, **10**, 4358–4392.
7 R. Akhter and S. S. Maktedar, *J. Materiomics*, 2023, **9**, 1196–1241.
8 G. Murali, J. Rawal, J. K. R. Modigunta, Y. H. Park, J.-H. Lee, S.-Y. Lee, S.-J. Park and I. In, *Sustainable Energy Fuels*, 2021, **5**, 5672–5693.
9 E. Sowbakkiyavathi, S. Arunachala Kumar, D. K. Maurya, B. Balakrishnan, J. Z. Guo and A. Subramania, *Adv. Compos. Hybrid Mater.*, 2024, **7**, 130.
10 S. Sahoo, G. Sahoo, S. M. Jeong and C. S. Rout, *J. Energy Storage*, 2022, **53**, 105212.
11 G. Wu, X. Wu, X. Zhu, J. Xu and N. Bao, *ACS Nano*, 2022, **16**, 10130–10155.
12 Z. Yan, S. Luo, Q. Li, Z. S. Wu and S. Liu, *Adv. Sci.*, 2024, **11**, 2302172.
13 M. Pantrangi, E. Ashalley, M. K. Hadi, H. Xiao, Y. Zhang, W. Ahmed, N. Singh, A. Alam, U. Younis and F. Ran, *Energy Storage Mater.*, 2024, **73**, 103791.
14 J. Xia, F. Chen, J. Li and N. Tao, *Nat. Nanotechnol.*, 2009, **4**, 505–509.
15 C. Liu, Z. Yu, D. Neff, A. Zhamu and B. Z. Jang, *Nano Lett.*, 2010, **10**, 4863–4868.
16 M. Naguib, M. Kurtoglu, V. Presser, J. Lu, J. Niu, M. Heon, L. Hultman, Y. Gogotsi and M. W. Barsoum, in *MXenes*, Jenny Stanford Publishing, 2023, pp. 15–29.
17 M. Jiang, D. Wang, Y. H. Kim, C. Duan, D. V. Talapin and C. Zhou, *Angew. Chem.*, 2024, **136**, e202409480.
18 N. Hemanth, T. Kim, B. Kim, A. H. Jadhav, K. Lee and N. K. Chaudhari, *Mater. Chem. Front.*, 2021, **5**, 3298–3321.

19 W. S. Poh, W. J. Yiang, W.-J. Ong, P. L. Show and C. Y. Foo, *J. Energy Chem.*, 2024, **91**, 1–26.
20 Z. A. Sheikh, P. K. Katkar, H. Kim, S. Rehman, K. Khan, V. D. Chavan, R. Jose, M. F. Khan and D.-K. Kim, *J. Energy Storage*, 2023, **71**, 107997.
21 S. A. Thomas, A. Patra, B. M. Al-Shehri, M. Selvaraj, A. Aravind and C. S. Rout, *J. Energy Storage*, 2022, **55**, 105765.
22 S. Mohapatra, H. T. Das, B. C. Tripathy and N. Das, *Chem. Rec.*, 2024, **24**, e202300220.
23 H. S. Jeong, G. Sahoo and S. M. Jeong, *Appl. Surf. Sci.*, 2024, **670**, 160622.
24 P. Bandyopadhyay, T. G. Senthamaraikannan, D.-H. Lim, G. Sahoo, E. Baasanjav, J.-K. Kim and S. M. Jeong, *Chem. Eng. J.*, 2024, **481**, 148578.
25 I. Hussain, C. Lamiel, M. S. Javed, M. Ahmad, S. Sahoo, X. Chen, N. Qin, S. Iqbal, S. Gu and Y. Li, *Prog. Energy Combust. Sci.*, 2023, **97**, 101097.
26 M. Sharma, P. M. Ajayan and P. Deb, *Adv. Mater. Interfaces*, 2023, **10**, 2202058.
27 F. Xing, G. Ji, Z. Li, W. Zhong, F. Wang, Z. Liu, W. Xin and J. Tian, *Mater. Horiz.*, 2023, **10**, 722–744.
28 J. Jin, T. Xiao, Y.-F. Zhang, H. Zheng, H. Wang, R. Wang, Y. Gong, B. He, X. Liu and K. Zhou, *Nanoscale*, 2021, **13**, 19740–19770.
29 C. Shen, L. Wang, A. Zhou, H. Zhang, Z. Chen, Q. Hu and G. Qin, *J. Electrochem. Soc.*, 2017, **164**, A2654.
30 J. Vyskočil, C. C. Mayorga-Martinez, K. Szőkölová, A. Dash, J. Gonzalez-Julian, Z. Sofer and M. Pumera, *ChemElectroChem*, 2019, **6**, 3982–3986.
31 M. Pathak and C. S. Rout, *Adv. Compos. Hybrid Mater.*, 2022, **5**, 1404–1422.
32 S. Radhakrishnan, M. Monisha, S. R. Ka, M. Saxena, S. M. Jeong and C. S. Rout, *Adv. Sustainable Syst.*, 2025, **9**, 2400529.
33 P. Siddu, S. Radhakrishnan, S. M. Jeong and C. S. Rout, *Batteries Supercaps*, 2025, **8**, e202400466.
34 C. Lamiel, I. Hussain, O. R. Ogunsakin and K. Zhang, *J. Mater. Chem. A*, 2022, **10**, 14247–14272.
35 C. Chen, X. Xie, B. Anasori, A. Sarycheva, T. Makaryan, M. Zhao, P. Urbankowski, L. Miao, J. Jiang and Y. Gogotsi, *Angew. Chem., Int. Ed.*, 2018, **57**, 1846–1850.
36 H. Wang, Z. Cui, S.-A. He, J. Zhu, W. Luo, Q. Liu and R. Zou, *Nano-Micro Lett.*, 2022, **14**, 189.
37 M. Pathak, P. Mane, B. Chakraborty and C. S. Rout, *J. Energy Storage*, 2023, **66**, 107475.
38 V. M. H. Ng, H. Huang, K. Zhou, P. S. Lee, W. Que, J. Z. Xu and L. B. Kong, *J. Mater. Chem. A*, 2017, **5**, 3039–3068.
39 Y. Bai, K. Zhou, N. Srikanth, J. H. Pang, X. He and R. Wang, *RSC Adv.*, 2016, **6**, 35731–35739.
40 P. Ghigna and E. Quartarone, *J. Phys. Energy*, 2021, **3**, 032006.
41 A. VahidMohammadi, J. Rosen and Y. Gogotsi, *Science*, 2021, **372**, eabf1581.
42 M. Okubo, A. Sugahara, S. Kajiyama and A. Yamada, *Acc. Chem. Res.*, 2018, **51**, 591–599.
43 M. Naguib, V. N. Mochalin, M. W. Barsoum and Y. Gogotsi, *Adv. Mater.*, 2014, **26**, 992–1005.
44 M. Khazaei, A. Ranjbar, M. Ghorbani-Asl, M. Arai, T. Sasaki, Y. Liang and S. Yunoki, *Phys. Rev. B*, 2016, **93**, 205125.
45 G. Berdiyorov, *Europhys. Lett.*, 2015, **111**, 67002.
46 Y. Ando, M. Okubo, A. Yamada and M. Otani, *Adv. Funct. Mater.*, 2020, **30**, 2000820.
47 Y. Sun, C. Zhan, P. R. Kent, M. Naguib, Y. Gogotsi and D.-E. Jiang, *ACS Appl. Mater. Interfaces*, 2019, **12**, 763–770.
48 A. Sugahara, Y. Ando, S. Kajiyama, K. Yazawa, K. Gotoh, M. Otani, M. Okubo and A. Yamada, *Nat. Commun.*, 2019, **10**, 850.
49 X. Ji, K. Xu, C. Chen, B. Zhang, Y. Ruan, J. Liu, L. Miao and J. Jiang, *Phys. Chem. Chem. Phys.*, 2016, **18**, 4460–4467.
50 W. Zhang, C. Cheng, P. Fang, B. Tang, J. Zhang, G. Huang, X. Cong, B. Zhang, X. Ji and L. Miao, *Phys. Chem. Chem. Phys.*, 2016, **18**, 4376–4384.
51 T. Shimada, N. Takenaka, Y. Ando, M. Otani, M. Okubo and A. Yamada, *Chem. Mater.*, 2022, **34**, 2069–2075.
52 J. Zhao, N. Ma, T. Wang, Y. Wang, B. Liang, Y. Zhang, S. Luo, Y. Xiong, Q. Wang and J. Fan, *Nanoscale Horiz.*, 2025, **10**, 78–103.
53 Z. Bo, Y. Chen, Q. Yu, J. Yan, K. Cen and Z. Liu, *J. Phys. Chem. C*, 2024, **128**, 2352–2361.
54 H. Shao, K. Xu, Y.-C. Wu, A. Iadecola, L. Liu, H. Ma, L. Qu, E. Raymundo-Piñero, J. Zhu and Z. Lin, *ACS Energy Lett.*, 2020, **5**, 2873–2880.
55 L. Xu and D.-E. Jiang, *J. Chem. Phys.*, 2021, **155**, 234707.
56 J. Wen, Q. Fu, W. Wu, H. Gao, X. Zhang and B. Wang, *ACS Appl. Mater. Interfaces*, 2019, **11**, 7087–7095.
57 A. Patra, S. Hegde, V. Mahamiya, B. Chakraborty, S. M. Jeong and C. S. Rout, *ACS Appl. Nano Mater.*, 2024, **7**, 11666–11679.
58 A. Sharma, P. Mane, B. Chakraborty and C. S. Rout, *ACS Appl. Energy Mater.*, 2021, **4**, 14198–14209.
59 A. Patra, P. Mane, K. Pramoda, S. Hegde, B. Chakraborty and C. S. Rout, *J. Energy Storage*, 2023, **68**, 107825.
60 S. Radhakrishnan, S. Lakshmy, K. S. Raj, B. Chakraborty, J. S. Cho, S. M. Jeong and C. S. Rout, *J. Energy Storage*, 2024, **99**, 113478.
61 R. Samal, P. Mane, S. Ratha, B. Chakraborty and C. S. Rout, *Energy Fuels*, 2022, **36**, 15066–15079.
62 S. R. Ka, N. Barman, K. Namsheer, R. Thapa and C. S. Rout, *Sustainable Energy Fuels*, 2022, **6**, 5187–5198.
63 S. Raj Ka, P. Mane, S. Radhakrishnan, B. Chakraborty and C. S. Rout, *ACS Appl. Nano Mater.*, 2022, **5**, 4423–4436.
64 S. R. Ka, N. Barman, S. Radhakrishnan, R. Thapa and C. S. Rout, *J. Mater. Chem. A*, 2022, **10**, 23590–23602.
65 T.-F. Yi, J.-J. Pan, T.-T. Wei, Y. Li and G. Cao, *Nano Today*, 2020, **33**, 100894.
66 R. Barik and P. P. Ingole, *Curr. Opin. Electrochem.*, 2020, **21**, 327–334.
67 A. Das, B. Raj, M. Mohapatra, S. M. Andersen and S. Basu, *Wiley Interdiscip. Rev.: Energy Environ.*, 2022, **11**, e414.
68 P. Kulkarni, S. Nataraj, R. G. Balakrishna, D. Nagaraju and M. Reddy, *J. Mater. Chem. A*, 2017, **5**, 22040–22094.
69 A. Choubey and A. Yadav, *J. Energy Storage*, 2024, **79**, 110131.
70 A. Patra and C. S. Rout, *J. Energy Storage*, 2023, **5**, e411.
71 H. Li, S. Lin, H. Li, Z. Wu, L. Zhu, C. Li, X. Zhu and Y. Sun, *J. Mater. Chem. A*, 2022, **10**, 7373–7381.
72 Y. Li, P. Kamdem and X.-J. Jin, *Dalton Trans.*, 2020, **49**, 7807–7819.
73 X. Liang, Y. Chen, Z. Jiao, M. Demir, M. Du and J. Han, *J. Energy Storage*, 2024, **88**, 111634.
74 A. Alam, K.-W. Kim, H. Jo, D. Sahoo, S. H. Kim, J. K. Kim and S. Lim, *J. Mater. Chem. A*, 2024, **12**, 13882–13889.
75 X. Chen, J. Cai, C. Qiu, W. Liu and Y. Xia, *Electrochim. Acta*, 2023, **438**, 141572.
76 H. Wang, L. You, Y. Guan, H. Wang, X. Ma, D. Wang, J. Wu, Y. Zhu, J. Lin and J. Liu, *Colloids Surf., A*, 2021, **629**, 127381.
77 A. Sharma and C. S. Rout, *Int. J. Energy Res.*, 2022, **46**, 24537–24553.
78 A. Sharma, A. Patra, K. Namsheer, P. Mane, B. Chakraborty and C. S. Rout, *J. Mater. Sci.*, 2021, **56**, 20008–20025.
79 H. Liu, R. Hu, J. Qi, Y. Sui, Y. He, Q. Meng, F. Wei, Y. Ren, Y. Zhao and W. Wei, *Adv. Mater. Interfaces*, 2020, **7**, 1901659.
80 Z. Pan, F. Cao, X. Hu and X. Ji, *J. Mater. Chem. A*, 2019, **7**, 8984–8992.
81 H. Liu, R. Hu, J. Qi, Y. Sui, Y. He, Q. Meng, F. Wei, Y. Ren and Y. Zhao, *Electrochim. Acta*, 2020, **353**, 136526.
82 Y. Luo, C. Yang, Y. Tian, Y. Tang, X. Yin and W. Que, *J. Power Sources*, 2020, **450**, 227694.
83 Y. Zhao, J. Guo, A. Liu and T. Ma, *J. Alloys Compd.*, 2020, **814**, 152271.
84 B. Kirubasankar, M. Narayanasamy, J. Yang, M. Han, W. Zhu, Y. Su, S. Angaiah and C. Yan, *Appl. Surf. Sci.*, 2020, **534**, 147644.
85 M. Chandran, A. Thomas, A. Raveendran, M. Vinoba and M. Bhagiyalakshmi, *J. Energy Storage*, 2020, **30**, 101446.
86 W. Hou, Y. Sun, Y. Zhang, T. Wang, L. Wu, Y. Du and W. Zhong, *J. Alloys Compd.*, 2021, **859**, 157797.
87 Z. Pan, X. Li, C. Yang and X. Ji, *J. Colloid Interface Sci.*, 2023, **634**, 460–468.
88 S. Hussain, D. Vikraman, Z. A. Sheikh, M. T. Mehran, F. Shahzad, K. M. Batoo, H.-S. Kim, D.-K. Kim, M. Ali and J. Jung, *Chem. Eng. J.*, 2023, **452**, 139523.
89 W. X. Cheng, Y. Z. Chen, S. Y. Liao, J. Q. Hu, C. S. Liu, S. F. Cui, X. W. Huang, Y. Liu and Y. Min, *ChemElectroChem*, 2022, **9**, e202200715.
90 P. T. Pınar, M. Gülcan and Y. Yardım, *J. Alloys Compd.*, 2024, **1010**, 177656.
91 X. Chen, J. Zhu, J. Cai, Y. Zhang and X. Wang, *J. Energy Storage*, 2021, **40**, 102721.
92 Y. Liu, G. Sahoo, E. M. Kim and S. M. Jeong, *Adv. Energy Sustainable Res.*, 2024, **5**, 2300234.
93 H. Jiang, Z. Wang, Q. Yang, L. Tan, L. Dong and M. Dong, *Nano-Micro Lett.*, 2019, **11**, 1–14.

94 C. Arulkumar, R. Gandhi and S. Vadivel, *Electrochim. Acta*, 2023, **462**, 142742.
95 S. Hussain, I. Rabani, D. Vikraman, T. Mehran, F. Shahzad, Y. S. Seo, H. S. Kim and J. Jung, *Int. J. Energy Res.*, 2021, **45**, 18770–18785.
96 S. Hussain, D. Vikraman, M. T. Mehran, M. Hussain, G. Nazir, S. A. Patil, H.-S. Kim and J. Jung, *Renewable Energy*, 2022, **185**, 585–597.
97 P. Zhou, L. Fan, J. Wu, C. Gong, J. Zhang and Y. Tu, *J. Alloys Compd.*, 2016, **685**, 384–390.
98 T. Kshetri, T. I. Singh, Y. S. Lee, D. D. Khumujam, N. H. Kim and J. H. Lee, *Composites, Part B*, 2021, **211**, 108624.
99 B. Ye, M. Huang, L. Fan, J. Lin and J. Wu, *J. Alloys Compd.*, 2019, **776**, 993–1001.
100 L. Pan, R. Hu, Y. Zhang, D. Sha, X. Cao, Z. Li, Y. Zhao, J. Ding, Y. Wang and Z. Sun, *Nano-Micro Lett.*, 2023, **15**, 225.
101 Z. Ye, Y. Jiang, L. Li, F. Wu and R. Chen, *Chem. Eng. J.*, 2022, **430**, 132734.
102 R. S. Kamat, C. U. Mulik, X. Wang, C. Padwal, A. A. Kulkarni, L. D. Jadhav and D. P. Dubal, *ChemNanoMat*, 2024, **10**, e202400384.
103 T. T. Mishra, M. Chakraborty, J. Behera and D. Roy, *Energy Fuels*, 2024, **38**, 9186–9217.
104 M. Pathak and C. S. Rout, *J. Electron. Mater.*, 2023, **52**, 1668–1680.
105 M. Patel, S. Patel, K. Mahabari, R. Mohili, A. H. Jadhav, M. Sharma, K. Lee and N. K. Chaudhari, *ACS Appl. Nano Mater.*, 2024, **7**, 28172–28185.
106 M. Pathak, S. Polaki and C. S. Rout, *RSC Adv.*, 2022, **12**, 10788–10799.
107 Y. A. Dakka, J. Balamurugan, R. Balaji, N. H. Kim and J. H. Lee, *Chem. Eng. J.*, 2020, **385**, 123455.
108 T. Li, Y. Liu, J. Wang, H. Hao, Z. Yu and H. Liu, *Chem. Eng. J.*, 2024, **487**, 150502.